Remote Sensing of Environment 304 (2024) 114026

Contents lists available at ScienceDirect

Remote Sensing of Environment

journal homepage: www.elsevier.com/locate/rse

Ecoregion-wise fractional mapping of tree functional composition in temperate mixed forests with sentinel data: Integrating time-series spectral and radar data

Ziyu Lin [a], K.H. Cheng [a], Dedi Yang [b], Fei Xu [c], Guangqin Song [a], Ran Meng [d], Jing Wang [e], Xiaolin Zhu [c], Michael Ng [f], Jin Wu [a,g,*]

[a] Research Area of Ecology and Biodiversity, School of Biological Sciences, The University of Hong Kong, Pokfulam, Hong Kong, China
[b] Environmental and Climate Sciences Department, Brookhaven National Laboratory, Upton, New York, USA
[c] Department of Land Surveying and Geo-Informatics, The Hong Kong Polytechnic University, Hong Kong, China
[d] College of Resources and Environment, Huazhong Agricultural University, Wuhan 430070, China
[e] School of Ecology, Shenzhen Campus of Sun Yat-sen University, Shenzhen, Guangdong, China.
[f] Department of Mathematics, Hong Kong Baptist University, Hong Kong, China
[g] Institute of Climate and Carbon Neutrality, The University of Hong Kong, Pokfulam, Hong Kong, China

ARTICLE INFO

Editor: Marie Weiss

Keywords:
Tree functional type
Spectral mixture analysis
Sentinel
SAR
Spatiotemporal variability
Google Earth engine

ABSTRACT

Temperate mixed forest ecosystems are composed of various tree functional types (TFTs) that differ in canopy structure, phenology, and physiological response to climate change. An accurate characterization of the composition of these TFTs is important for quantifying land surface carbon, energy, and water cycling, as well as process-based simulation of forest dynamics. However, because the pixel size of satellite imagery is usually larger than temperate tree crowns, it is challenging to untangle the significant pixel-wise signal mixture of TFT across mixed forest regions. Spectral Mixture Analysis (SMA) has been widely used to derive the sub-pixel fractional composition of TFT from satellite imagery, but accounting for the broad spectral variability within TFTs across space and time remains a challenge. Synthetic aperture radar (SAR) can indicate biomass mixture information, but it has not been fully exploited for deriving subpixel TFT composition. To improve TFT composition mapping in mixed forest regions, we developed a Fisher-transformation-based Spectral and Radar Time-series Mixture Analysis (F-SRTMA) framework on Google Earth Engine. The F-SRTMA framework aims to address the space-time TFT variability of satellite signatures based on two modified modules: (1) the use of spectral and radar data with spatial and temporal information, and (2) feature optimization based on Fisher Discriminant Analysis (FDA). We tested the F-SRTMA at three representative temperate mixed landscapes located in the northeastern United States, where time-series Sentinel-1 and -2 data were used to calibrate our F-SRTMA approach. Airborne hyperspectral and LiDAR-derived canopy height data were used to generate ground reference TFT fraction maps for validation. The results demonstrate that (1) compared to the spectral time-series model, the synergy of spectral and radar time-series features yielded higher accuracy at the local sites (r^2 = 0.649 vs. 0.680); (2) optimized feature based on FDA significantly minimized the within-TFT variability while maximizing the between-TFT variability, which further improved model generalizability across different landscapes, yielding the highest accuracy with cross-site r^2 increasing from 0.634 to 0.715 and RMSE decreasing from 0.207 to 0.164. Collectively, these results suggest that F-SRTMA can be an accurate and generalizable approach for sub-pixel fraction mapping across temperate mixed landscapes, with the potential to be applied to other mixed forest ecosystems.

1. Introduction

Temperate mixed forest ecosystems are known for their heterogeneity, with their functioning significantly regulated by the diversity of plant species (Anderegg et al., 2018; Espelta et al., 2020; Jung et al., 2021; Van Der Plas et al., 2016). Different groups of tree species

* Corresponding author at: School of Biological Sciences, The University of Hong Kong, Pokfulam Road, Hong Kong, China.
E-mail addresses: linziyu@connect.hku.hk (Z. Lin), jinwu@hku.hk (J. Wu).

https://doi.org/10.1016/j.rse.2024.114026
Received 30 May 2023; Received in revised form 28 January 2024; Accepted 31 January 2024

often exhibit distinct structural, physiological, and phenological traits that govern many important ecological processes related to plant functions (Díaz and Cabido, 2001; Ustin and Gamon, 2010). Therefore, the composition of Tree Functional Types (TFTs) has often been used as a crucial indicator of forest functional diversity. Improving monitoring of TFT composition across environmental gradients is essential for better understanding the dynamics of mixed forests in relation to TFT functioning in carbon, energy, and water cycling, particularly under climate change (Cooley et al., 2022; Han et al., 2022; Poulter et al., 2015).

The global accessibility of spaceborne observations has facilitated large-scale TFT monitoring (Van Cleemput et al., 2021). However, the relatively coarse spatial resolution of publicly available satellite imagery, such as Moderate-resolution Imaging Spectroradiometer (MODIS, 500 m), Landsat (30 m), and Sentinel-2 (10-20 m) (Claverie et al., 2018; Sousa and Davis, 2020), presents challenges for accurately monitoring TFTs due to the widely evident TFT mixture in mixed forest ecosystems. The pixel size of these satellite images is typically much larger than the size of temperate tree crowns (e.g., crown diameter oftentimes is smaller than 10 m; Wu et al., 2021; Zhao et al., 2022a), leading to a pronounced mixed pixel problem where the spectral reflectance of a single pixel originates from a combination of different TFTs (Quintano et al., 2012). As a result, accurate characterization of TFT mixture processes using satellite remote sensing remains challenging, particularly in temperate regions where landscapes often comprise heterogeneous combinations of TFT due to the fragmented land forms and associated complex interactions of vegetation with climate, topography, and disturbance histories over large geographical areas (Box and Fujiwara, 2015).

Generally, spectral mixture algorithms (SMA) have been used to effectively address the mixed pixel problem, in which individual image pixels are explicitly modeled as combinations of pure land cover signals, also known as endmembers (Settle and Drake, 1993; Shimabukuro and Smith, 1991). However, due to the high inter-class similarity of TFT spectra, the limited number of bands (typically 4–12 bands) in satellite-based multi-spectral imagery constrains the model's unmixing capability (Sousa and Davis, 2020; Wang et al., 2021). The recent advances in satellite remote sensing, such as Sentinel-2 with an increased temporal resolution, has created new opportunities to differentiate tree types by capturing their distinct phenology and physiological seasonal variability (Claverie et al., 2018). This has led to a focus on improving unmixing effectiveness based on the accumulation of dense multi-temporal imagery (spectral time-series mixture analysis, STMA), instead of relying on mono-date imagery (Gómez et al., 2016). The addition of time-series imagery has been demonstrated to significantly improve TFT fractional mapping for different unmixing models, including semi-empirical models (i.e., vegetation indies-based dimidiate pixel model; Gao et al., 2020; Yang et al., 2021) and physics-based models (i.e., linear/non-linear mixture model; Hemmerling et al., 2021; Nill et al., 2022; Schug et al., 2020; Sousa and Davis, 2020; Wang et al., 2021; Zhuo et al., 2022), as well as machine learning (data-driven) models (Bolyn et al., 2022; Okujeni et al., 2021; Senf et al., 2020).

Despite these advances, current techniques for unmixing TFT fractions are exclusively based on spectral-only mixture models. These models can struggle to differentiate spectrally similar vegetation types, or fail to describe TFT variations due to uneven illumination in mountainous regions (Mendes et al., 2019; Waser et al., 2021). To tackle this issue, earlier studies have integrated radar imagery with spectral imagery for discrete TFT classifications which resulted in enhanced accuracy (Waser et al., 2021), indicating that this integration could be beneficial in improving the accuracy of TFT mixture analysis. Satellite-based radar data with wavelength at centimeter scale display distinct energy intensity that is related to vegetation surface roughness (Giordano et al., 2018; Li et al., 2019) and can be sensitive to seasonal changes in forest structure, such as the defoliation of deciduous trees (Dostálová et al., 2018; Ling et al., 2022; Tanase et al., 2019; Verheghghen et al., 2022). This is because the volume backscattering mechanism is intrinsically linked to canopy structure and biomass dynamics in space and time, with great potential to help improve the spectral-only unmixing models given its ability to estimate plant biophysical properties, such as vegetation biomass or leaf area index (Englhart et al., 2011; Joshi et al., 2015). Similar to spectral mixture analysis, radar-based scattering mixture algorithms are effective in modeling scattering mixture mechanisms from land cover types with different structural attributes (Freeman and Durden, 1998; Giordano et al., 2018; Singh et al., 2019). Such radar-based mixture analyses have been widely used for land cover identification such as snow, ice, or water but have been underexplored for TFT fractional mapping (Arii et al., 2019; Ferguson and Gunn, 2022; Hillebrand et al., 2022; Parida and Mandal, 2020; Tian and Wang, 2022).

To aid in the integration of spectral and radar time-series unmixing, Sentinel-1 is a particularly advantageous satellite source as it provides concurrent time-series radar data with Sentinel-2 multi-spectral data (Malenovský et al., 2012). This combination offers an unprecedented opportunity to assess the individual and combined impacts of spectral and structural information on TFT fractional mapping accuracy. Meanwhile, the growing support of high computational cloud platforms with vast preloaded geospatial datasets and parallel processing capacity, such as Google Earth Engine, offers novel and timely opportunities for multi-source data reconstruction, facilitating large-scale mapping (Gorelick et al., 2017).

When conducting large-scale TFT fractional mapping, the use of time-series and multi-source satellite data can provide more comprehensive information than mono-date or spectral-only data. However, this increased data complexity may introduce insubstantial noise or unrepresentative bands into the unmixing process, which could ultimately affect the model's generalizability across large landscapes. This noise amplification in satellite imagery can be attributed to factors such as cloud and snow cover, shadows, topographic effects, and speckle for radar data, all of which contribute to increased spatial and temporal variability of spectral and/or radar features within TFT and reduce the between-TFT feature contrasts (Wang et al., 2021; Zhao et al., 2022b; Zhuo et al., 2022). Moreover, the environmental gradient across large scales can also enhance the within-TFT spectral and structural variability, which further reduces the endmember representativeness across space and time (Hemmerling et al., 2021; Sousa and Davis, 2020). To minimize the effect associated with this space-time variability in large-scale unmixing models, researchers often employ either (1) endmember selection to improve endmember library representativeness or (2) band features optimization to improve feature representativeness (Somers et al., 2011). While the former approach solely focuses on accounting for variable mixture conditions with respect to within-TFT variability, the latter approach is more effective because it could suppress the effect from both within-TFT and between-TFT endmember variability (Jin et al., 2010; Liu et al., 2017; Xu et al., 2019). One possible solution to the latter approach is Fisher Discriminant Analysis (FDA; Okada and Tomita, 1985). This kind of supervised data transformation method can convert high-dimensional data inputs into a low-dimensional feature space, where between-class endmember variability is maximized while within-class endmember variability is minimized, thus generating more representative features for complex landscapes. Several recent studies also have demonstrated the great effectiveness of the FDA in resolving the model transferability issue in impermeable surface monitoring (Liu et al., 2017; Ouyang et al., 2022; Xu et al., 2019). However, its ability to improve endmember generalizability in TFT fractional mapping remains underexplored.

The goal of this study is to explore whether the Fisher-transformation-based Spectral and Radar Time-series Mixture Analysis (F-SRTMA) framework can be an effective and accurate way to improve TFT fraction monitoring in temperate mixed forests across large landscapes using Sentinel-1 and -2 time-series imagery. To address the space-time variability of TFT signatures across large heterogeneous landscapes, the F-SRTMA framework utilizes both spatial and temporal information from spectral and radar data and performs an additional

feature optimization based on FDA. As our focus, we tested the F-SRTMA at a representative temperate mixed forest ecoregion located in Wisconsin, USA, and aimed to answer the following two questions:

1) To what extent could the integration of spectral and radar time-series imagery improve the accuracy of TFT fractional mapping?
2) Will the embedding of FDA with SRTMA help increase model generalizability across different landscapes?

2. Study sites, materials, and methods

2.1. Study sites

This study focused on the northern upland conifer-hardwood mixed forest ecoregion in Wisconsin, United States, which experiences a continental climate, characterized by long, cold winters and short, warm growing seasons. The mean annual temperature of the ecoregion is approximately 3 °C, and the mean annual precipitation is around 800 mm (Mackay et al., 2002). The ecoregion is mosaicked by a dynamic composition of deciduous and evergreen TFT, including deciduous broadleaf hardwoods, evergreen conifers, deciduous conifers, shrubs, and grasses. Based on the differences in leaf habit (evergreen and deciduous) and leaf forms (broadleaf and needle-leaf), we grouped temperate tree species into three types of interest: deciduous broadleaved tree (DBT), evergreen needle-leaved tree (ENT), and deciduous needle-leaved tree (DNT). The remaining land covers were grouped as non-forest (nonF) class and water (W) class.

Within this ecoregion, we selected three sites (Fig. 1) from the National Ecological Observatory Network (NEON) to evaluate our proposed F-SRTMA method. These sites are the University of Notre Dame Environmental Research Center (UNDE, 46.21° N, 89.51° W), Steigerwaldt (STEI, 45.50° N, 89.50° W), and Chequamegon (CHEQ, 45.81° N, 90.08° W).

We chose these sites for two reasons. First, each of them has unique site characteristics that are representative of the TFT compositional complexity and space-time feature variability across the ecoregion, as they differ considerably in terms of hydrological regime (UNDE), disturbance history (STEI) and topography (CHEQ) according to the NEON site description (https://www/.neonscience.org/field-sites). Specifically, UNDE has many scattered small lakes surrounded by wetlands, with deciduous conifers dominating most of the wetlands. Thus, the background water signal would affect the remotely sensed vegetation signal from space. STEI is a site with intensive human interruption, and the landscape is also composed and contaminated by the remote sensing signals associated with seasonal crops, urban areas, and plantations. CHEQ exhibits relatively complex topographic conditions that affect the illumination and radar backscatter observed from space. As such, these sites and their associated unique site characteristics can serve as an excellent testbed not only for testing the accuracy of our proposed method but also for helping to examine the generalizability issue of the proposed method when applying the method developed at one site to other sites. Secondly, relevant 'ground truth' data to evaluate our remote sensing methods is available at these sites. NEON has conducted annual airborne surveys since 2015, with a very high spatial resolution (1 m) airborne hyperspectral and LiDAR imagery. These airborne data would generate accurate classification results, serving as 'ground truth' to evaluate our remote sensing methods in a wall-to-wall manner.

2.2. Materials

We used three types of data in this study: (1) airborne hyperspectral and LiDAR data, (2) Sentinel optical reflectance (Sentinel-2) and radar (Sentinel-1) data, and (3) auxiliary land cover maps (from NEON airborne products and several land cover products).

2.2.1. Airborne hyperspectral imagery and canopy height products

To validate our F-SRTMA method, we used high-resolution (1 m) airborne hyperspectral images and canopy height product (level 1) data acquired from the NEON Airborne Observation Platform (Kampe et al.,

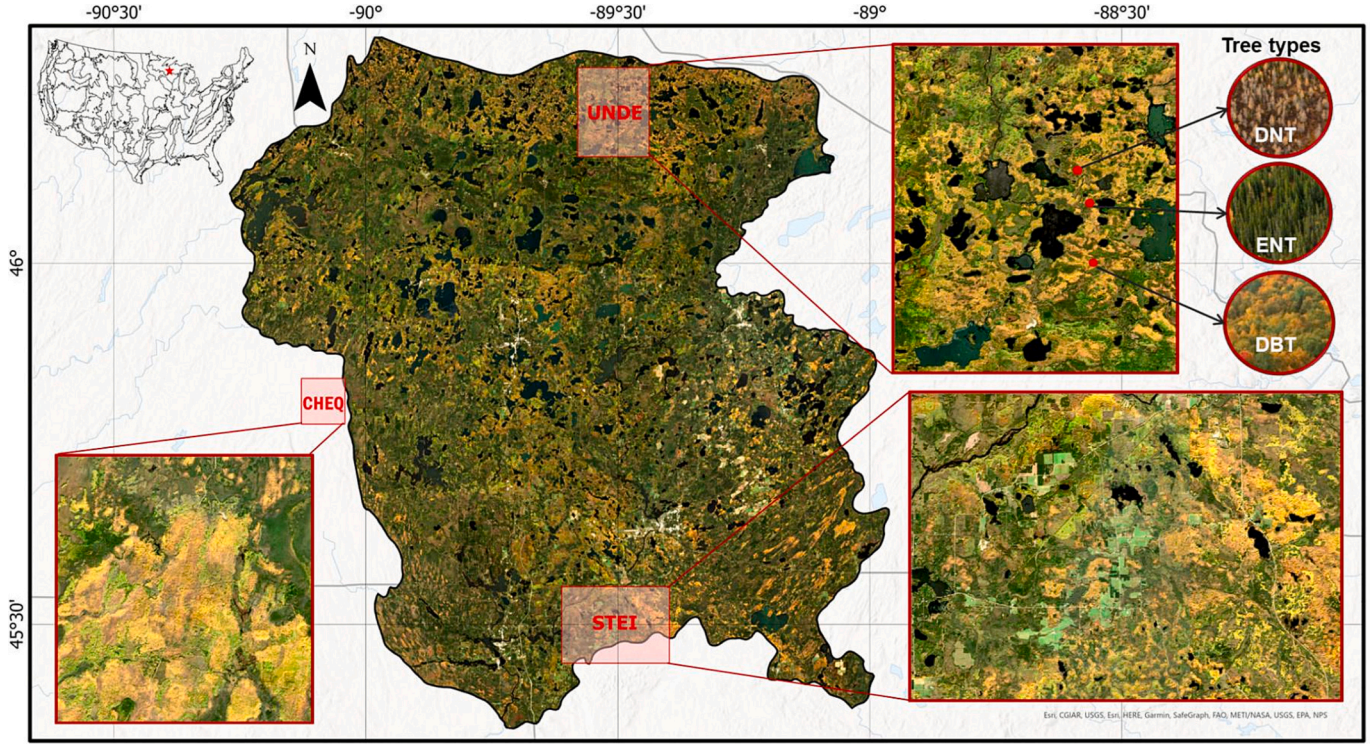

Fig. 1. The autumn land surface condition (using Sentinel-2 R-G-B composite image) within the Wisconsin northern upland mixed forest ecoregion, featuring three distinct validation sites (UNDE, CHEQ, and STEI) and three target tree types (DNT, ENT and DBT) for fraction estimation purpose.

2010). The hyperspectral image data consists of 426 bands ranging from 380 to 2510 nm with a 5 nm spectral resolution. We downloaded the data for the year 2020 from https://data.neonscience.org/ to match with Sentinel satellite imagery. We employed a spectral-spatial residual network (SSRN) deep learning model, specifically a 3D-CNN model (Zhong et al., 2018), to classify each landscape pixel into three tree types (i.e., DBT, DNT, ENT)and a non-forested type (nonF). We chose the SSRN model for its ability to handle high collinearity commonly existing in spectroscopic data and its delivery of state-of-the-art classification performance (Zhong et al., 2018).

There were two steps involved in the SSRN classification. First, to create training and validation data, we manually labeled different land cover types (total pixel amount = 1.62×10^6, DBT = 7.91×10^5, ENT = 2.71×10^5, DNF = 1.22×10^5, nonF = 4.35×10^5) based on sub-meter historical winter and summer images of the same sites from the ESRI World Imagery Wayback archive (https://livingatlas.arcgis.com/wayback) and Sentinel-2 winter imagery. Second, to train and evaluate the SSRN model, we followed Wong and Yeh (2020) and used a 5-fold cross-validation method with both airborne hyperspectral imagery and canopy height map as model input. To balance the contribution of spectral and structure information to the classification model, we reduced the hyperspectral data from the original 426 bands to 10 bands using the Minimum Noise Fraction method (MNF; Roger, 1996) (Fig. S1). The resulting classification had a very high overall accuracy of ~0.93 (Table S1), indicating that it can be a reliable benchmark to evaluate satellite-based fraction estimations. To evaluate satellite-derived TFT fractions (at a 10 m resolution), we further resampled these 1 m resolution classifications and upscaled them to generate a 10 m resolution fractional composition of our targeted TFT (i.e., DBT, DNT, ENT, and nonF).

2.2.2. Optical and radar sentinel data

To test our F-SRTMA method, we used the Sentinel-2 Multispectral Instrument data operated by the European Space Agency. Specifically, the Sentinel-2 level 2 A imagery with a 5-day revisit time covering the full year of 2020 was accessed via the Google Earth Engine (GEE). We selected four 10 m spectral bands (blue, green, red, and near-infrared bands) and six 20 m spectral bands (3 red-edge, 1 near-infrared and 2 short-wave infrared bands) and fused them to a 10 m resolution using the nearest neighbor method. To minimize snow and cloud contamination, we first excluded imagery in the snowy season from December to March, as well as imagery with >50% cloud coverage based on the provided CLOUDY_PIXEL_PERCENTAGE parameter. Then, for the remaining imagery, we filtered cloudy pixels based on Sentinel-2 cloud probability bands (i.e., cloud probability>10%), and snow-contaminated pixels based on a thresholding method (i.e., NDSI>0) using Normalized Difference Snow Index (NSDI) following Gascoin et al. (2019). In addition, to minimize solar and sensor view angle effects, we conducted an image-specific Bidirectional Reflectance Distribution Function (BRDF) normalization following the same method as Claverie et al. (2018). We also performed a path length correction algorithm to minimize the topography effects following Yin et al. (2018).

In addition, we accessed Sentinel-1 Level 1 Ground Range Detected (GRD) imagery with a 12-day revisit time covering the full 2020 year via GEE. Sentinel-1 GRD imagery provides backscatter coefficients (σ°) in decibels (dB) based on the Interferometric Wide Swath mode, with a 10 m resolution and dual-polarization signals (i.e., vertical transmit-vertical receive, VV, and vertical transmit-horizontal receive, VH). Since the values of backscattering coefficients (σ°_{VV} and σ°_{VH}) typically vary with the incidence angles (ranging from 29° to 46°), we normalized both the σ°_{VV} and σ°_{VH} values to a reference angle of 38° based on a dynamic cosine model (Feng et al., 2021) to reduce this effect. Then, we followed Mullissa et al. (2021) to convert the dB values of σ°_{VV} and σ°_{VH} to linear power unit as $10^{\sigma\circ/10}$ (ranging from 0 to 0.3). To minimize the effect of topography, we utilized the US 10 m resolution Digital Elevation Model on GEE for terrain correction, following the method of Vollrath et al. (2020). We also reduced the speckle based on a refined-Lee filter with a 5 × 5 pixel window, following Yommy et al. (2015). Although Sentinel-1 data are insensitive to atmospheric conditions, its information can be contaminated by wet underground and snow cover (Dostálová et al., 2018), leading to significant data uncertainty during snowmelt and wet seasons. To eliminate these related extreme values and outliers, we implemented pixel-wise outlier detection based on a 5-year time-series (2018–2022) of two polarizations (VV and VH) in both snow and wet seasons. This method removes observations outside the interquartile range, which is the lower 10% to upper 90% quantiles of the two polarizations, respectively.

2.2.3. Auxiliary land cover data

To evaluate the advantage of fraction mapping on ecoregion-wise TFT, we cross-compared our results with another two discrete classification maps of non-forest type based on two published land cover data: WorldCover 2020 (WC) land cover products with a 10 m resolution (Zanaga et al., 2022) and Global Forest Canopy Height 2019 (GCH) with a 30 m resolution (Potapov et al., 2021). WC is a land cover product generated based on the Sentinel-2 and Sentinel-1 constellations, with demonstrated high accuracy globally (Zanaga et al., 2022). The product can be accessed via https://worldcover2020.esa.int/. GCH was developed through an integration of the Global Ecosystem Dynamics Investigation (GEDI) LiDAR data and Landsat analysis-ready time-series data with satisfactory accuracy (Potapov et al., 2021). This product can be accessed via https://glad.umd.edu/dataset/gedi/. We created two binary maps of forest and non-forest based on the 'Tree cover' type of WC and pixels with canopy height > 3 m from GCH, respectively. We converted these two discrete maps into fraction format by resampling their spatial resolution to 90 m. Both maps demonstrated a moderately strong correlation with the airborne LiDAR-derived nonF benchmark at three validation sites, exhibiting correlation coefficients of 0.740 and 0.757, respectively. These two forest maps were used as an independent comparison product for our estimated ecoregion-wise forest fraction map (Section 3.5 and 4.3).

2.3. Methods

The F-SRTMA framework includes three main tasks. First, a data fusion approach is conducted to reconstruct spectral-radar time-series (SRT) features that minimize noise over time and improves feature comparability across sites. Second, the endmembers are extracted based on ground reference and a spatial-guided purity metric is used to constrain imagery-wise endmember extraction. Third, FDA is conducted on the extracted endmembers and associated SRT features, aiming to increase the feature contrast (i.e., minimizing intra-TFT variability and maximizing inter-TFT variability) and thus improve the feature representativeness across large regions.

2.3.1. Reconstruction of high-quality SRT features

There are two issues to be addressed in constructing high-quality SRT features for unmixing models: 1) data missing across time-series images associated with cloud/snow contamination, and 2) signal anomalies across the time frame caused by environmental factors such as topography and weather or sensor/preprocessing errors. Existing time-series unmixing models address these issues by using only clear-sky satellite time series (Wang et al., 2021; Zhuo et al., 2022). However, this approach limits model generalizability as clear-sky images collected at a specific combination of time stamps are not always available at different sites or across different years. To make SRT features applicable on a broad scale, we developed a method to gap-fill Sentinel time series data and derive SRT features with even time intervals. Details about the reconstruction method are described below.

To resolve the data missing or anomalies across Sentinel-1 and -2 data time series due to the quality-controlled processes in Section 2.2.2,

we applied a pixel-wise gap-filling method on each spectral band with three sub-steps. First, we calculated the median value for each time-stamp based on 5-year (2018–2022) Sentinel-1 and -2 data, respectively. Second, for each target pixel in 2020 with a missing value, we gap-filled it with the 5-year median value of the corresponding time stamp if available. Third, if the valid median value was unavailable, we used the monthly average as a reasonable proxy of that pixel in 2020 for gap-filling. To further minimize potential data anomalies, we imposed a 2-order Savitzky–Golay filter following Chen et al. (2004) with a 2-order linear regression smoother at a 7-week window. Lastly, to keep the time interval consistent across different locations, we resampled the Sentinel-1 and -2 data into a monthly median format (Table 1).

2.3.2. Extractions of candidate endmember pixels

The representativeness of endmembers directly impacts sub-pixel fractional mapping accuracy (Roth et al., 2012). Identifying high-quality endmembers in temperate mixed forests from satellite imagery is particularly challenging, due to the substantial variability in spatial and temporal remote sensing signals within TFTs and the broad spectral similarity between TFTs, which are influenced by phenological diversity and environmental factors. To address these challenges associated with our spectral-radar time series features, we turned to spatial-guided endmember finding methods, which are highly appliable for diverse remote sensing features and large landscapes due to their unsupervised nature (e.g., Mei et al., 2010; Shi and Wang, 2014).

In this study, we investigated an automatic morphological endmember extraction method (Plaza et al., 2002). This method utilizes the morphological eccentricity index (MEI), a spatial-guided purity index, to extract endmember candidates. We encountered challenges when using the default MEI index for TFT purity estimation. The default MEI method defines the degree of purity based on the spectral distance between mixed and pure pixels in the neighborhood. While the spectral distance method works well for differentiating land covers that have significantly different spectra, such as forests and water bodies, it becomes less effective for distinguishing between different TFTs that have relatively small spectral differences (Fig. S2b). To address the limitations of the default MEI method in differentiating TFTs with similar spectral characteristics, we adopted a two-step preprocessing before MEI calculation: 1) removing non-vegetation land covers to focus only on vegetated surfaces; 2) maximizing feature variation of vegetation by using Principal Component Analysis (PCA)(Jolliffe, 2011). Our further analysis confirmed that the PCA-based MEI method is indeed more effective in searching pure pixels compared to the MEI based on the original remote sensing features (Figs. S2b *vs.* S2c). In detail, our endmember extraction process includes the following four steps:

Step 1: Derive a vegetation-specific PCA map to enhance the sensitivity of MEI to TFTs. We first removed non-vegetation land covers based on a NDVI threshold (yearly medium NDVI <0.5)(Carlson and Ripley, 1997). Then, we performed a PCA analysis on the spectral-radar time series imagery focusing only on the remaining vegetation pixels, generating a vegetation-specific PCA map to enhance the contrast between TFTs.

Table 1
Time-series Sentinel −1 and −2 features used in Spectral and Radar Time-series Mixture Analysis.

Satellite	Band selection	Spatial resolution (m)	Acquisition time	Temporal resolution	No. of feature
Sentinel-1	VV, VH	10	2020.04–2020.11	Monthly average	16 (=2 × 8)
Sentinel-2	B2-B4, B8	10	2020.04–2020.11	Monthly average	32 (=4 × 8)
	B5-B7, B8A, B11, B12	20	2020.04–2020.11	Monthly average	56 (=7 × 8)

Step 2: Derive a PCA-MEI map to extract the endmember candidates. Following Plaza et al. (2002), for each image pixel, we applied two mathematical morphology operators, dilation and erosion, to the first three components of the vegetation-specific PCA map. Dilation selects the brightest pixel, and erosion selects the darkest pixel in the N × N pixel neighborhood of PCA map. MEI is calculated as the feature angle distance (FAD; Eq. (1)) between the dilation and the erosion map, with a higher MEI indicating a higher degree of "eccentricity" compared to its neighbors and thus a higher likelihood of the pixel's purity. Based on the calculated MEI map, we created the candidate endmember map using the Otsu method (Otsu, 1979), with the derived threshold T_{MEI} set to 0.78 and the endmember candidate map determined by MEI > T_{MEI}.

$$MEI = FAD(A,B) = cos^{-1}\left(\frac{AB}{\|A\|\|B\|}\right) = cos^{-1}\left(\frac{\sum_{i=1}^{n} A_i B_i}{\sqrt{\sum_{i=1}^{n} A_i A_i}\sqrt{\sum_{i=1}^{n} B_i B_i}}\right) \quad (1)$$

where A and B denote the 1×3 vector from PCA-based dilation and erosion maps respectively; n denotes the amount of neighbor pixels within the N × N search window.

Notably, the MEI index requires both pure and mixed pixels to coexist within neighboring kernels, also known as the transition region of two land covers. If the search window is not large enough to cover this "transitioning" from purity to mixtures, such as in homogenous regions, MEI could underestimate pixel purity (Plaza et al., 2002). In order to capture a wider range of mixture gradients and enhance recognition in both homogeneous and transition regions, we followed the approach outlined by Plaza et al. (2002). By increasing the search window size, we observed improved results, as depicted in Figs. S2c and S2d. To determine the optimal window size, we conducted a sensitivity test and found that an N × N window size of 41 × 41 pixels yielded the best performance, as shown in Fig. S2e. It's worth noting that when applied this method to other landscapes, the optimal search radius size can be automatically approximated based on the variogram range of spatial autocorrelation analysis (Yang et al., 2023).

Step 3: Endmember type determination. After identifying the candidate endmember pixels, we overlaid the candidate map of each site with its corresponding airborne-derived TFT fraction map (Section 2.2.3) to assign each candidate pixel to its dominant endmember class. In addition to TFTs, non-forest (nonF) endmembers were determined based on canopy height data (CHM < 3 m), while water endmembers were selected using a NDWI threshold (yearly median NDWI >0.05) (McFeeters, 1996).

Step 4: Construction of the SRT endmember library. To account for potential large within-class endmember variability, we followed Xu et al. (2019) and extracted multiple endmembers (sub-class) for each land cover type. Specifically, we used the K-means clustering method for automatically identifying sub-classes. The resulting endmember bundle, which includes K endmembers (sub-classes) for each land cover type, was used as the final endmember library. Since the number of K could affect the final unmixing results, we conducted a sensitivity analysis to determine the optimal K value. In this analysis, K ranged from 1 to 15 with an interval of 2, and the model's performance was assessed using airborne-derived TFT fraction maps. Fig. S3 illustrates that K = 7 and K = 1 achieved optimal performance for the model without and with FDA, respectively.

2.3.3. SRT-based mixture analysis (SRTMA)

(1) MESMA

We estimated TFT fractions based on an advanced unmixing model—Multiple Endmember Spectral Mixture Analysis (MESMA) (Roberts et al., 1998), which has been demonstrated to effectively cope with within-class endmember variability (Degerickx et al., 2019). This is because MESMA allows using varied endmember combinations for each

pixel instead of a fixed one. This assumption can better cope with reality, where the number of mixture types at a 10 m resolution is typically around three, which is much less complex than the number of the entire endmember library (Okujeni et al., 2021). To perform MESMA, we searched for the most representative 3-endmember combinations for each mixed pixel by iterating through all possible 3-endmember combinations from the library. For each iteration of the 3-endmember subset, we used pixel-wise linear spectral mixture analysis (Eq. (2)) to estimate the subpixel abundance.

$$\boldsymbol{Y} = \boldsymbol{XA} + \boldsymbol{e} \tag{2}$$

where $\boldsymbol{Y}$ is $n \times 1$ vector of features for each pixel; $\boldsymbol{X}$ is the $n \times m$ matrix of endmembers; n (=number of feature bands; Table 1) and m (=3; endmembers selected from the library) denote the number of feature bands and endmembers, respectively. $\boldsymbol{e}$ is the systematic error/model residual. $\boldsymbol{A}$ is the $m \times 1$ vector of the estimated abundances, which is solved based on a least-squares optimization algorithm (Bro and Jong, 1997), and the derived abundances are subject to the "sum-to-one constraint" and "non-negativity constraint" (Heinz and Chein-I-Chang, 2001). Among the abundances estimated for different endmember subsets, we selected the abundance estimate from the best model with the lowest residual to obtain the final TFT-specific abundance.

(2) FDA-based MESMA

To optimize endmember representativeness, we applied a supervised dimensionality reduction method known as Fisher's discriminant analysis (FDA) to transform the SRT features into Fisher features. The FDA method was chosen for its effectiveness in enhancing the inter-class endmember variability while reducing the intra-class endmember variability, as demonstrated in previous studies (Liu et al., 2017; Ouyang et al., 2022; Xu et al., 2019). Our aim was to address the challenge of low model generalizability across different sites while making little-to-no sacrifice on within-site model accuracy. For detailed information on the mathematics underlying the FDA method, interested readers can refer to Xu et al. (2019).

Here, we implemented FDA using three sub-steps. First, we utilized the previously derived endmember library as input for FDA to identify projection directions that would optimize the distance between data points of different endmember classes when minimizing the distance within each class. This resulted in a Fisher transformation projection vector $\boldsymbol{V} = \{v_1, v_2, \ldots, v_{k-1}\}$, with a dimension of $(k\text{-}1) \times n$ (where n is number of the features, k is the number of endmember types and in this study $k = 5$). Second, we transformed the original features into k-1 Fisher features based on projection vector $\boldsymbol{V}$. By applying this feature dimensional reduction, Eq. (2) was converted into Eq. (3), as shown below.

$$\boldsymbol{VY} = \boldsymbol{VXA} + \mathbf{e} \tag{3}$$

where $\boldsymbol{V}$ refers to the FDA projection vector, while $\boldsymbol{A}$, $\boldsymbol{X}$, $\boldsymbol{Y}$ and $\boldsymbol{e}$ are the same as those shown in Eq. (2).

In a pixel-wise iterative procedure, we searched for the best estimate in the obtained Fisher feature space. By solving the abundance vector $\boldsymbol{A}$ in Eq. (3) for each of the 3-endmember combinations following Heinz and Chein-I-Chang (2001), we chose the combination with the lowest model residual $\boldsymbol{e}$ to determine the corresponding land cover types and their abundances. This process was conducted on a pixel basis for the whole image.

2.3.4. Analytical experiments and model evaluations

To examine the accuracy and cross-site generalizability of F-SRTMA, we conducted four analyses. The first analysis aimed to assess the separate and joint contributions of spectral, radar, and temporal features to the accuracy of TFT fractional mapping. We compared the MESMA models with different features as model inputs, including 1) Spectrum of the annual median (mono-S), 2) Radar Time-series (RT), 3) Spectral Time-series (ST), 4) Spectral and Radar Time-series (SRT), and 5) Fisher features derived from Spectral and Radar Time-series (FDA-SRT). To evaluate inter- and intra-site performance with comparable settings, for each site, we conducted an independent 3-fold spatial cross-validation. For this, we divided each site into 2 km × 2 km sub-tiles, which were split into three groups, with each group being used iteratively for unmixing and validation while the other two groups were reserved for endmember extraction.

The second analysis aimed to examine whether the FDA method suppresses feature space-time variability and improves cross-site model generalizability. For this purpose, we first compared the within-class and between-class feature variability within the FDA and PCA space. Then, we compared two modeling scenarios with and without FDA for different feature combinations.

The third analysis aimed to evaluate the model's generalizability across large landscapes. We designed a non-local-based endmember scenario, in which a site-specific endmember library was first extracted and then applied to the other two sites. We conducted non-local endmember scenarios for different feature combinations across three sites, and compared the accuracy of the non-local scenarios with the local-based endmember scenarios from the second analysis.

The fourth analysis aimed to upscale F-SRTMA for TFT fractional mapping across the entire ecoregion in Fig. 1. We coded our F-SRTMA method on GEE, from which we derived the ecoregion map of TFT fractions. To demonstrate the necessity of fractional mapping in heterogeneous landscapes, we cross-compared the derived non-forested (nonF) fractions with two state-of-the-art non-forest products (WC and GCH) on the ecoregion scale.

We used benchmark data from the airborne-derived TFT fraction map for validation. We employed four widely-used validation metrics in unmixing studies (Nill et al., 2022; Powell et al., 2007; Senf et al., 2020): Root Mean Square Error (RMSE), square of correlation coefficient (r^2), coefficient of determination (R^2), and the slope and intercept of a regression line. RMSE quantifies the absolute model error, r^2 and R^2 quantify the goodness-of-fit in models, and slope and intercept indicate the model systematic error and bias. The validation data were evenly sampled from low to high fraction intervals (i.e., 0.1–0.2, 0.2–0.3, …,0.9–1.0), with 100 randomly sampled pixels per fraction interval. Note that potential geolocation errors in Sentinel imagery can add up to >12 m and introduce noise and associated uncertainties when validating, and the downscaling of 20-m Sentinel-2 bands to 10-m also introduce the observational errors for pixel-wise unmixing models. This is especially pronounced for those TFTs with rare-to-subdominant abundance (Cohen et al., 1990; Schubert et al., 2017). To balance out uncertainties from potential geolocation errors across different datasets and spatial scales of different bands, we followed Wang et al. (2023) to conduct validation at patch level (i.e., the mean value at a 90 m × 90 m square area). We further conducted a sensitivity analysis on the evaluation accuracy across a range of patch sizes from 30 m to 110 m with an interval of 20 m. Our findings indicate that 90 m is the optimal size as it minimizes geolocation errors between different data sources (Fig. S4).

3. Results

3.1. Temporal patterns of TFT endmembers

Our analysis of endmembers' seasonal patterns (Fig. 2) reveals that different bands in the Sentinel-2 sensor capture various ecological dynamics, including seasonal changes in leaf color, quantity, and potential leaf biochemistry, and these ecological dynamics vary considerably across TFTs. For instance, broadleaf forests generally exhibit higher concentrations of chlorophyll, resulting in a lower reflectance in the red band compared to needleleaf forests. Additionally, the highly clumped structure of coniferous forests leads to lower overall reflectance for ENT and DNT compared to DBT.

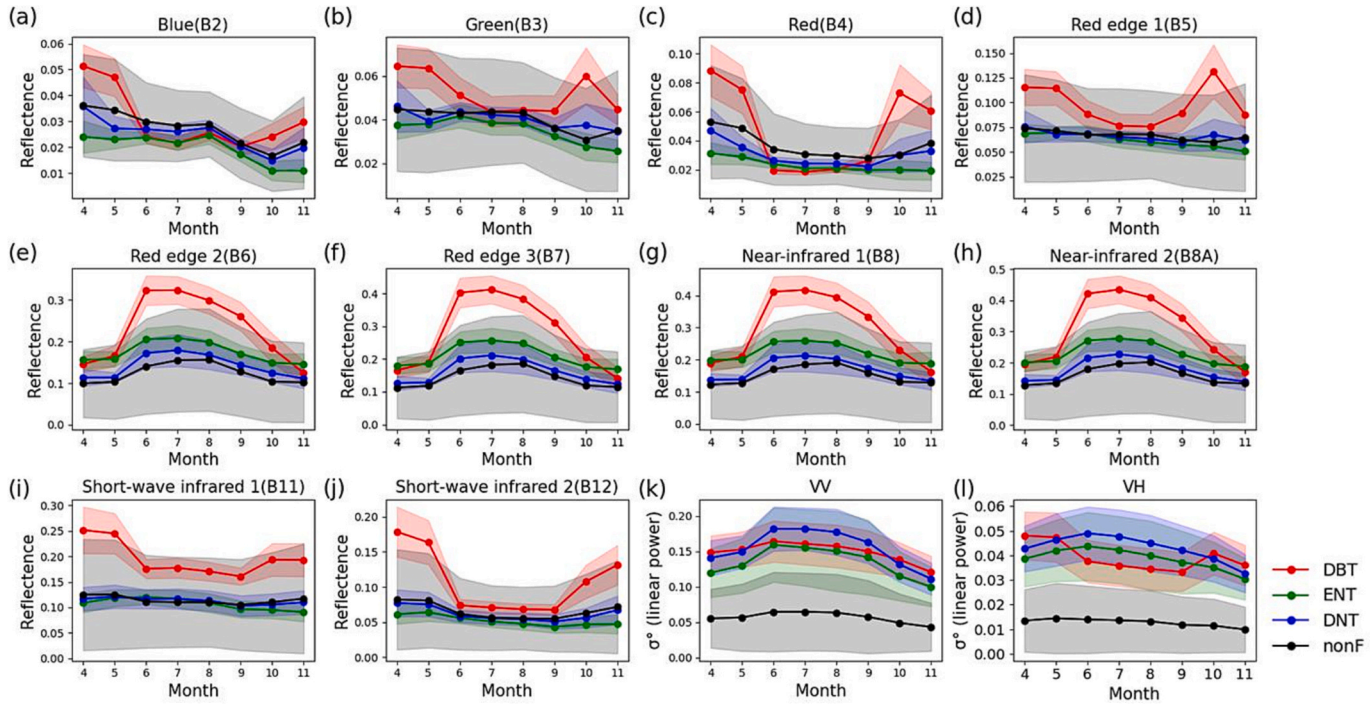

Fig. 2. Seasonal patterns for endmembers on a monthly timescale from April to November, including means (in lines) and standard deviations (in color shading), across various Sentinel-2 and Sentinel-1 bands. Sentinel-2 bands are represented as follows: (a) visible blue, (b) visible green, (c) visible red, (d) red edge 1, (e) red edge 2, (f) red edge 3, (g) near-infrared 1, (h) near-infrared 2, (i) short-wave infrared 1, and (j) short-wave infrared 2. Sentinel-1 bands are depicted as (k) VV, and (l) VH. (For interpretation of the references to color in this figure legend, the reader is referred to the web version of this article.)

In terms of seasonal reflectance patterns, DBT and DNT exhibit more pronounced reflectance seasonality in visible and near-infrared bands, indicating the phenological changes in leaf color and leaf quantity (e.g., leaf on/off) on the ground that can be sensed by Sentinel-2 satellites. ENT reflectance also exhibits a smaller (and moderate) degree of seasonality across most bands. The seasonality of the red-edge and near-infrared bands (B6-B8A) is almost identical, indicating a strong relationship between these bands in capturing changes related to vegetation growth, health, and senescence. Furthermore, the reflectance of TFT endmembers shows significant overlaps with that of nonF type, suggesting that distinguishing TFTs solely based on spectral information can be challenging due to their similar spectral characteristics.

Regarding SAR patterns, we observed that both VV and VH polarizations are sensitive to surface structures (Fig. 2k and l). The nonF type in SAR data exhibits greater separability compared to the Sentinel-2 bands (Fig. 2a-h). In terms of canopy scattering, conifer trees display higher values in both VV and VH bands compared to broadleaf trees. The volume scattering between DNT and ENT is nearly comparable, with DNT exhibiting higher values than ENT, indicating higher tree density for DNT compared to ENT. Additionally, DBT exhibits distinct seasonal patterns in VH while showing less significant seasonal patterns in VV values, which can be attributed to VH being more sensitive to randomly oriented structures, such as tree canopies, while VV is more responsive to linearly oriented structures like surfaces and trunks(Flores-Anderson et al., 2019).

3.2. *Evaluating the effectiveness of SRT features for TFT fractional mapping*

We investigated the performance of different feature combinations on sub-pixel TFT fractional mapping. Among the four non-FDA feature scenarios examined (Table 2), SRT features yielded the highest overall accuracy (RMSE = 0.176, r^2 = 0.680) across all study sites, followed by ST (RMSE = 0.180, r^2 = 0.649), RT (RMSE = 0.210, r^2 = 0.576), and mono-S (RMSE = 0.222, r^2 = 0.550). We found that the contribution of different features to unmixing is different at the TFT level (DBT, DNT, and ENT). For instance, radar time-series data were found to be the most capable of identifying the cover of DBT, but less efficient for differentiating ENT and DNT (r^2 = 0.694, 0.577 and 0.427). Unlike radar time-series, spectral time-series data were more effective at estimating ENT, followed by DBT and DNT (r^2 = 0.736, 0.717 and 0.501).

The combined use of spectral and radar time series (SRT) resulted in a further increase in overall accuracy compared to spectral time (ST) features alone. This improvement is evident in the increase of r^2 from

Table 2
Accuracy statistics of fraction estimations using different feature combinations, including mono-date Spectral (mono-S), Radar Time-series (RT), Spectral Time series (ST), Spectral and Radar Time series (SRT), and FDA-transformed SRT (FDA-SRT) features. The accuracy values were calculated from the average of 9 independent within-site runs (3-fold evaluation per site). The overall results were calculated from the accuracy of all land covers per column.

Land cover	RMSE					r^2				
	mono-S	RT	ST	SRT	FDA-SRT	mono-S	RT	ST	SRT	FDA-SRT
DBT	0.265	0.192	0.183	0.173	0.128	0.517	0.694	0.717	0.739	0.826
DNT	0.219	0.199	0.185	0.178	0.163	0.545	0.427	0.501	0.559	0.641
ENT	0.178	0.235	0.161	0.161	0.153	0.642	0.577	0.736	0.736	0.766
nonF	0.227	0.213	0.189	0.193	0.154	0.494	0.608	0.641	0.685	0.783
Overall	0.222	0.210	0.180	0.176	0.150	0.550	0.576	0.649	0.680	0.754

0.649 to 0.680, and the decrease in RMSE from 0.180 to 0.176. The addition of radar information proved its particular benefits for DBT and DNT (RMSE decreased from 0.183 to 0.173, and 0.185 to 0.178), but with an exception for ENT (RMSE remained consistent at 0.161). In contrast to TFT fractional cover, the mapping accuracy of nonF cover decreased with the integration of spectral and radar features (RMSE = 0.189 vs. 0.193 for ST and SRT features; Table 2). This suggests that the constructed SRT endmember library was not robust against the significantly high within-nonF variability.

3.3. Evaluating the effectiveness of FDA features

To evaluate the effectiveness of FDA in optimizing the endmember variability between different TFTs, we compared the dimensional reduction of SRT features based on FDA with PCA (Fig. 3). Our findings revealed a significant decrease in the similarity among different endmembers when using FDA, as compared to PCA, suggesting that FDA features offer improved representativeness (Fig. 3a and c). Specifically, when comparing the first four features of PCA and FDA results (Fig. 3b vs. d), we found that PCA features of the nonF type exhibited the much higher within-class variability compared to TFTs and its endmember candidates have significant overlap regions with all three TFTs. In contrast, FDA features of the nonF type displayed less within-class variability and a larger distance to TFTs. Additionally, ENT and DNT were highly similar in the PCA features but distinct in the FDA features (Fig. 3b and d). This optimization for within- and between-class variability explains the accuracy increment in models using FDA-SRT features compared with SRT features in the within-site experiments (RMSE = 0.150 vs. 0.176 and $r^2 = 0.754$ vs. 0.680; Table 2). Notably, the nonF type experienced the most significant decrease in with-class variability, resulting in the highest increase in r^2 of 0.098, followed by DBT with an increase of 0.087, DNT with an increase of 0.082, and ENT with a marginal increase of 0.030(Table 2).

Overall, the FDA analysis reduced the original feature dimensions to a much smaller dimension ($n = 180$ vs. 4), resulting in improved fractional mapping accuracy and computational efficiency. Notably, our results demonstrate that the FDA features, characterized by reduced within-class variability, enabled the model to achieve high accuracy using only one endmember for each land cover type. In contrast, non-FDA models typically require a more extensive endmember library to represent the considerable variability across diverse landscapes (Fig. S3). This highlights the efficiency and effectiveness of the FDA approach in reducing the complexity of endmember selection while maintaining high unmixing accuracy. It is equally important to note that some minor variation in the FDA model's performance occurs as the number of sub-endmembers increases. This variation in the FDA model is likely associated with the adverse effects of high collinearity between the sub-endmembers due to the reduction of within-class variability (Chen et al., 2011; Sabol et al., 1992). Therefore, the collinearity issue should be considered when implementing FDA analysis in future studies with similar objectives.

3.4. Evaluating the cross-site model generalizability

We aimed to investigate whether the utilization of different feature scenarios could improve the representation of cross-site endmembers, thereby improving model generalizability (Table 2 vs. Table 3). In ST feature scenario, we observed a significant reduction of overall accuracy for cross-site models compared to the within-site models ($r^2 = 0.570$ vs.0.649, RMSE = 0.222 vs.0.180). This indicates that models using ST features lack generalizability when applied to large landscapes. In the cross-site scenario, ST features can adequately simulate DBT and ENT to

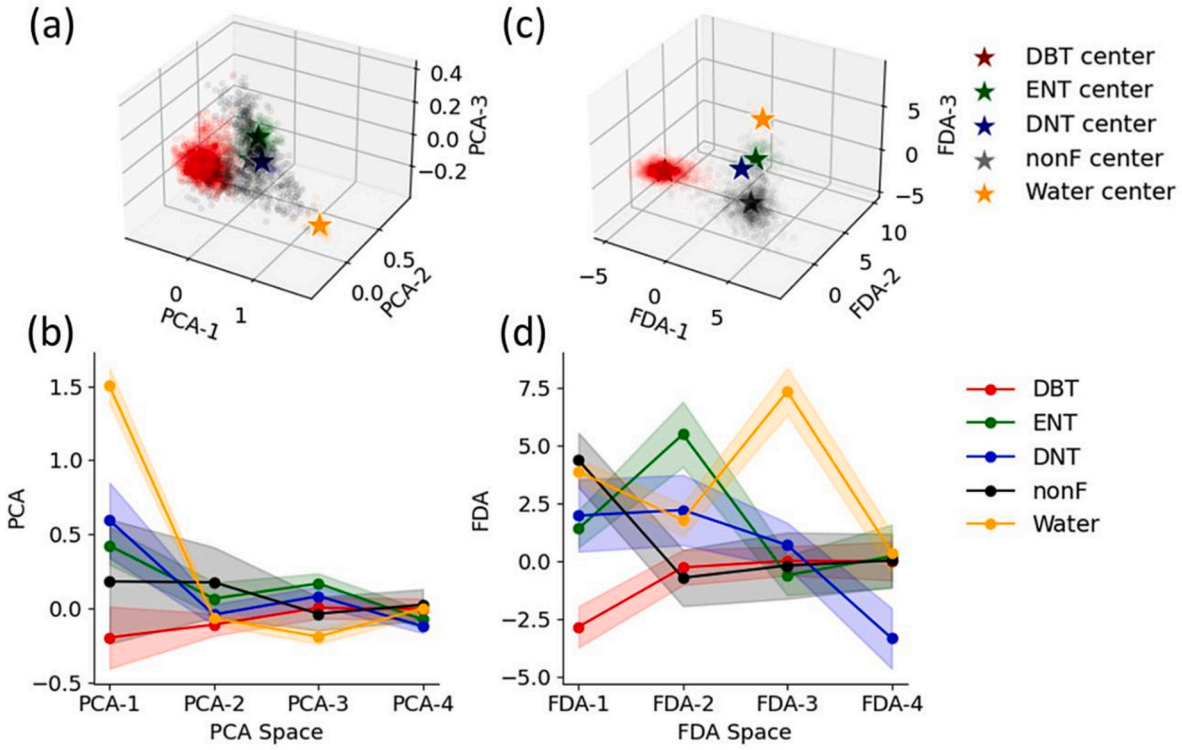

Fig. 3. Reduced within-class variability and increased between-class variability of SRT endmembers after Fisher discriminant analysis (FDA). The figure includes 3D scatter plots and dimensionally reduced feature patterns of endmember candidates based on PCA and FDA respectively. Panels (a) and (b) depict the endmember candidates in the PCA feature space, while panels (c) and (d) show the endmember candidates in the FDA feature space. The stars in the 3D scatter plots represent the K-means clustering centers corresponding to different land types, and the distance between cluster centers infers the between-class variability. In the lower panels, error bars present the standard deviation of endmember candidates for both PCA features and FDA features, indicating within-class variability for the non-FDA and FDA-based endmembers.

Table 3
Evaluation of cross-site endmember generalizability under different feature combination scenarios, including FDA-transformed Spectral Time series (FDA-ST), and FDA-transformed Spectral and Radar Time series (FDA-SRT) features. The average accuracy and corresponding standard deviation are reported for each land cover category, with 6 cross-site models (2 runs for each site) considered. The evaluations were performed on a 90 m patch scale.

	RMSE				r^2			
	ST	SRT	FDA-ST	FDA-SRT	ST	SRT	FDA-ST	FDA-SRT
DBT	0.210 ± 0.019	0.210 ± 0.023	0.127 ± 0.017	0.123 ± 0.017	0.647 ± 0.108	0.667 ± 0.106	0.805 ± 0.053	0.817 ± 0.048
DNT	0.263 ± 0.077	0.195 ± 0.034	0.274 ± 0.051	0.201 ± 0.027	0.389 ± 0.201	0.556 ± 0.123	0.467 ± 0.082	0.536 ± 0.082
ENT	0.185 ± 0.039	0.190 ± 0.042	0.168 ± 0.046	0.171 ± 0.039	0.724 ± 0.059	0.715 ± 0.055	0.762 ± 0.080	0.765 ± 0.075
nonF	0.231 ± 0.054	0.235 ± 0.044	0.162 ± 0.022	0.163 ± 0.018	0.518 ± 0.145	0.598 ± 0.103	0.697 ± 0.134	0.742 ± 0.072
Overall	0.222 ± 0.056	0.207 ± 0.039	0.183 ± 0.066	0.164 ± 0.038	0.570 ± 0.184	0.634 ± 0.112	0.683 ± 0.158	0.715 ± 0.127

some extent ($r^2 = 0.647$ and 0.724, RMSE = 0.210 and 0.185) but poorly represent the DNT($r^2 = 0.389$, RMSE = 0.263). Moreover, the class-wise accuracy is unstable (overall standard deviation of $r^2 = 0.184$). In this regard, the addition of radar time-series data (i.e., SRT features) is of utmost importance due to its impact on enhancing both cross-site accuracy for DNT ($r^2 = 0.556$, RMSE = 0.195) and the stability of class-wise performance (overall standard deviation of $r^2 = 0.112$).

We next explored the potential benefits of incorporating FDA to mitigate the adverse effects in increased within-class variability in space-time features caused by large landscapes, and thus increase the cross-site model generalizability (Figs. 4 and 5). The SRT endmembers exhibited low cross-site generalizability, indicated by lower accuracy and larger model uncertainties compared to the within-site evaluations for all land types (as depicted by the error bars in Fig. 4). The use of FDA-SRT endmembers resolved this deficiency and yielded consistently high accuracy under both local and non-local scenarios, and the overall accuracy for both within- and cross-site evaluations was more comparable ($r^2 = 0.754$ vs. 0.715, RMSE =0.164 vs. 0.150; Table 2 vs. Table 3). We observed that the combination with FDA analysis could lead to a substantially improved accuracy and model stability, especially for nonF type ($r^2 = 0.598 \pm 0.103$ vs. 0.742 ± 0.072 for SRT and FDA-SRT features).

Regarding model bias, as shown by the fitting red line in Fig. 6, the non-FDA model tends to overestimate DBT and DNT where they are less abundant (fraction<0.4 for SRTMA and fraction<0.3 for F-SRTMA) while underestimating the fractions where they are dominant. Similarly, for ENT and nonF, the models tend to underestimate their fractions across the fraction gradient. Nevertheless, the scatter plots show a significant decrease in bias when incorporating FDA into the SRTMA model.

3.5. Ecoregion-wise mapping and cross-comparison with discrete non-forest products

To demonstrate the effectiveness of the F-SRTMA approach for mapping forest/non-forest fractions across large and diverse landscapes, we conducted a cross-comparison of the nonF fractions on a 90 m patch level derived using the F-SRTMA approach with two nonF classification products (WC and GCH). The comparison revealed a strong correlation between the fraction maps derived from F-SRTMA and those from the other two products across the ecoregion (0.740 for WC and 0.759 for GCH). However, upon closer examination of the spatial patterns, we found that the two discrete maps tended to underestimate non-forested extents compared to our nonF fraction map, especially in areas where the physical sizes of ground objects (i.e., roads, streams, canopy gaps) are smaller than those of satellite image pixels (Fig. 8). In contrast, our proposed F-SRTMA approach was able to accurately capture these fine-scale land cover types, providing more precise sub-pixel level information.

4. Discussion

Mapping TFT fractions at a large scale is critical to understanding the composition and functional response of temperate mixed forests to changing climates. However, it remains challenging for satellite-based approaches to achieve high accuracy and cross-site generalizability. In our study, we proposed the F-SRTMA framework, which addresses these challenges with two novel aspects: (1) higher accuracy of TFT fractional mapping achieved by assimilating more feature dimensions (i.e., spectral, radar and temporal; SRT) compared to the conventional SMA and STMA methods that rely on the spectral features only, and (2) improved cross-site model generalizability achieved by further integrating FDA

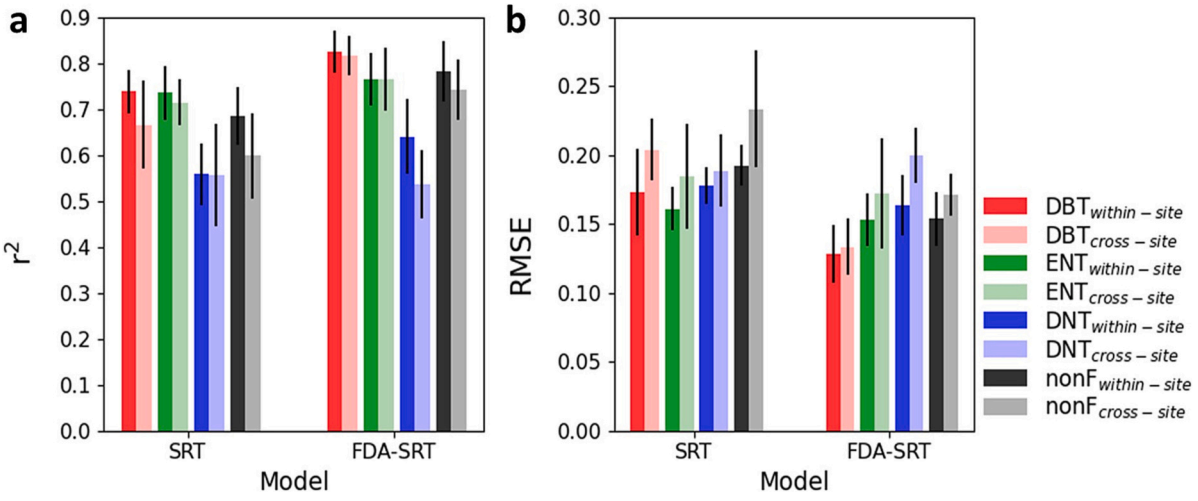

Fig. 4. Comparison of model performance in terms of both (a) r^2 and (b) RMSE using local (within-site) and non-local (cross-site) endmembers based on SRT and FDA-SRT features. For the within-site case, error bars indicate the standard deviation of accuracy across three sites. In the cross-site case, error bars display the average and uncertainties derived from 9 within-site models (three runs per site) and 6 cross-site models (two runs per site).

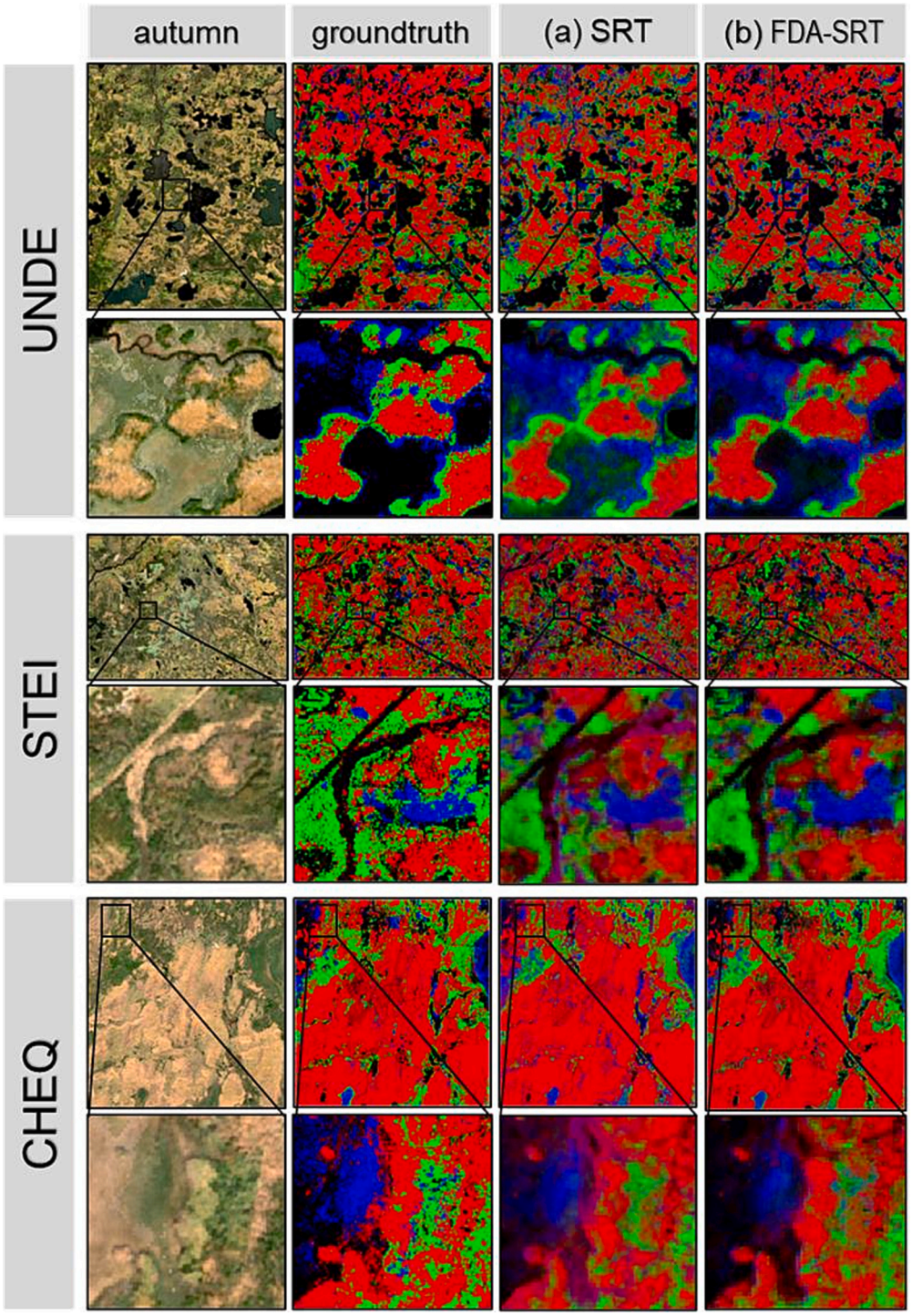

Fig. 5. Fraction maps showcasing cross-site endmember generalizability. The independent site was mapped using non-local endmembers with spectral-radar time-series (SRT) and FDA-SRT features, respectively. Sentinel-2 autumn RGB images are provided for reference. Ground truth fraction maps were derived from 1 m airborne TFT classification. Estimated class fraction scaled from [0,1] with red, green, blue and black corresponding to the DBT, ENT, DNT, and non-F type, respectively. (For interpretation of the references to color in this figure legend, the reader is referred to the web version of this article.)

with SRT features.

4.1. Effectiveness of the F-SRTMA framework in advancing the TFT fractional mapping

Distinct and representative features are critical for accurate spectral unmixing analysis and thus TFT fractional mapping. We found that the combined use of time-series spectral reflectance and radar signatures could be a way to improve unmixing accuracy. First, the inclusion of time-series spectral information provided a more comprehensive representation of TFT ecological characteristics and dynamics, such as seasonal variations in leaf color, biochemistry, and quantity (Wu et al., 2018; Wu et al., 2021; Yang et al., 2014). In contrast, limited spectral information inherent in mono-date multi-spectral imagery (Wang et al., 2021) typically leads to the "spectral mimicking" issue, where different TFTs may sometimes display similar spectra (Adams and Gillespie,

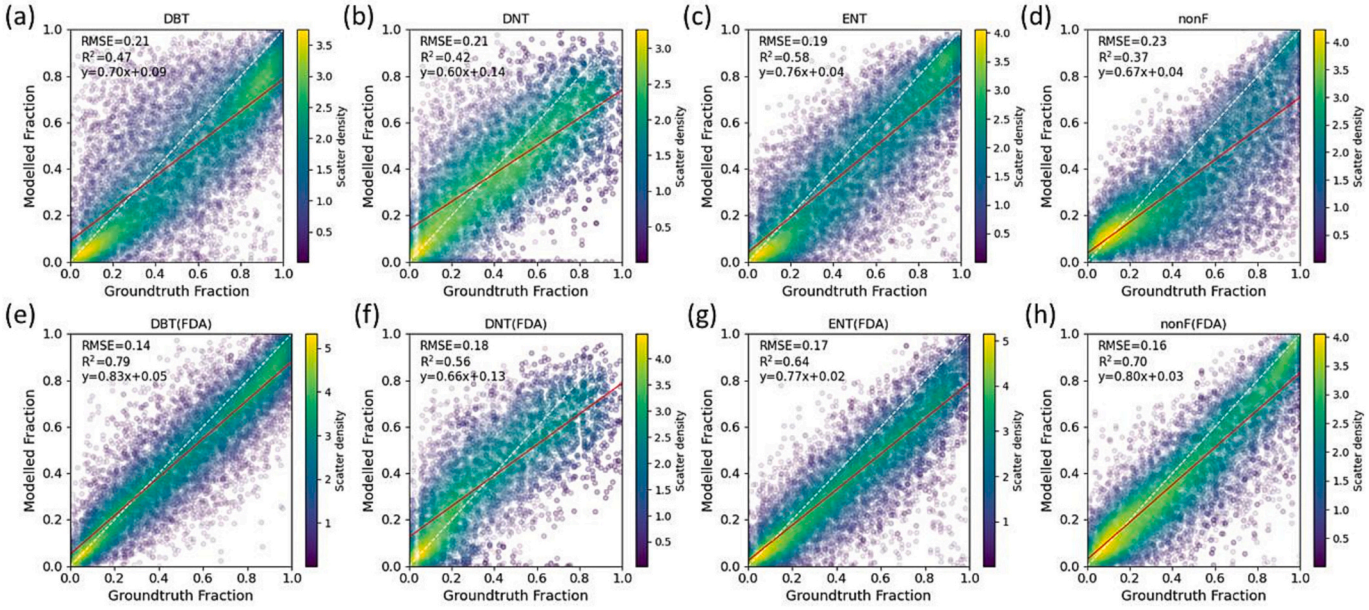

Fig. 6. Scatter plots for cross-site tests based on SRTMA and F-SRTMA models. The upper panels display the results of the SRTMA model, while the lower panels show the results of the F-SRTMA model. The scatters represent the estimates from all cross-site models, where for each model we randomly sampled 100 fraction estimates within each 0.1 interval.

2006; Sousa and Davis, 2020). Thus, compared to mono-date spectral mixture analysis models, time-series spectral information increased the separability among different TFTs and yielded superior TFT fractional mapping results (Table 2).

Second, our study demonstrated that time-series radar information further enhanced the separability among TFTs and other vegetations, particularly for those with considerable differences in canopy structure (e.g., DNT vs. DBT, tree vs. grass; Fig. 2k and l) (Sousa and Davis, 2020). Specifically, we observed that the endmember candidates of the nonF type exhibited significant spectral band overlap with DNT but were more distinguishable in the VV and VH bands (Fig. 2). Thus, the RT features significantly enhanced their differentiation and resolved the "spectral mimicking" effects between nonF and TFTs and yielded higher accuracy (Table 2). We also noticed that the RT features is only a complement to the ST features. For example, the DBT displayed a distinct temporal pattern in the ST features (especially in red-edge to near infrared bands), consequently, incorporating the RT features did not show significant complement to its differentiation. In contrast, EBTs and ENTs can present a similar "spectral mimicking" in ST features, particularly in lower latitude regions where EBTs and ENTs coexist with higher tree species diversity. While we did not examine EBTs within the model, in this case, the differences in canopy structure of broadleaf and needleleaf trees inferred from SAR data, could potentially help differentiate between coexisting broadleaf and conifer trees (i.e., EBT vs. ENT; DBT vs. DNT). Therefore, a comprehensive evaluation of the broader-scale applicability of our proposed method, as well as the identification of necessary adjustments for enhancing scalability, remains essential in future endeavors.

Notably, our study examined SAR time-series signals for unmixing models for the first time. The clear physical meaning of backscatter signals aligns with the principles of time-series spectral mixture (Arii et al., 2019), enabling the use of SAR data to model the fractional mixture of volume scattering dynamics within tree canopies (Waser et al., 2021). For instance, backscatter signals from broadleaved trees exhibited higher values in both polarizations during the leaf-off period compared to the leaf-on period (Reiche et al., 2018; Tanase et al., 2019), which is useful in distinguishing tall trees from low vegetation such as shrubs and grass. However, we also observed that assimilating RT data in a linear mixture model also introduce uncertainty, as the improvement of SRT over ST features is marginal or even negative for some TFTs (Table 2). This can be attributed to the inherent multi-scattering processes in SAR data and its significantly stronger nonlinear mixture relationship, which deviates from the linear assumption in linear mixture models. Taking this drawback into account, our model only utilized SAR data as a complementary source to the optical information and used FDA to further mitigate the limitations posed by multi-scattering effects.

To further assess the impact of multi-scattering effects on linear mixture models, we mapped the residuals of the linear mixture model with radar time-series (RT) features (Fig. S5). In most of the forest regions, the residuals are relatively small, indicating that the multi-scattering effects in forest regions are not significant (Fig. S5a). This could because the weaker penetration capability of C-band (5.547 cm) is dominantly responsive to the volume scattering from canopy while the trunks and ground scattering can be negligible, as demonstrated in several previous studies (Freeman and Durden, 1998; Schmullius and Evans, 1997). We showcased three examples of high residual regions for RTMA model in Fig. S5. Example 1 shows that model failed to capture the ground-trunk scattering at forest boundary; example 2 shows the surface scattering from the wetland; and example 3 shows the canopy (volume) scattering from the dense needle evergreen trees). Despite these high residuals, the RTMA-based fraction map demonstrates strong spatial consistency with the ground truth map (Figs. S5c and S5d), indicating that these residuals do not significantly impact the estimated TFT fractions. This result thus offers valuable insights into the effectiveness of radar time-series for differentiating between different various tree types, which could potentially enhance the accuracy of TFT fractional mapping.

4.2. Enhanced model generalizability for broader-scale TFT fractional mapping

The lack of generalizability can limit the usefulness of the model for large-scale mapping applications, where accurate and consistent results across different areas and time are critical. To address this issue, we integrated FDA with SRT features to improve the representativeness of the TFT endmember library across complex vegetation landscapes (Fig. 7a vs. Fig. S7). The inclusion of higher feature dimensions often

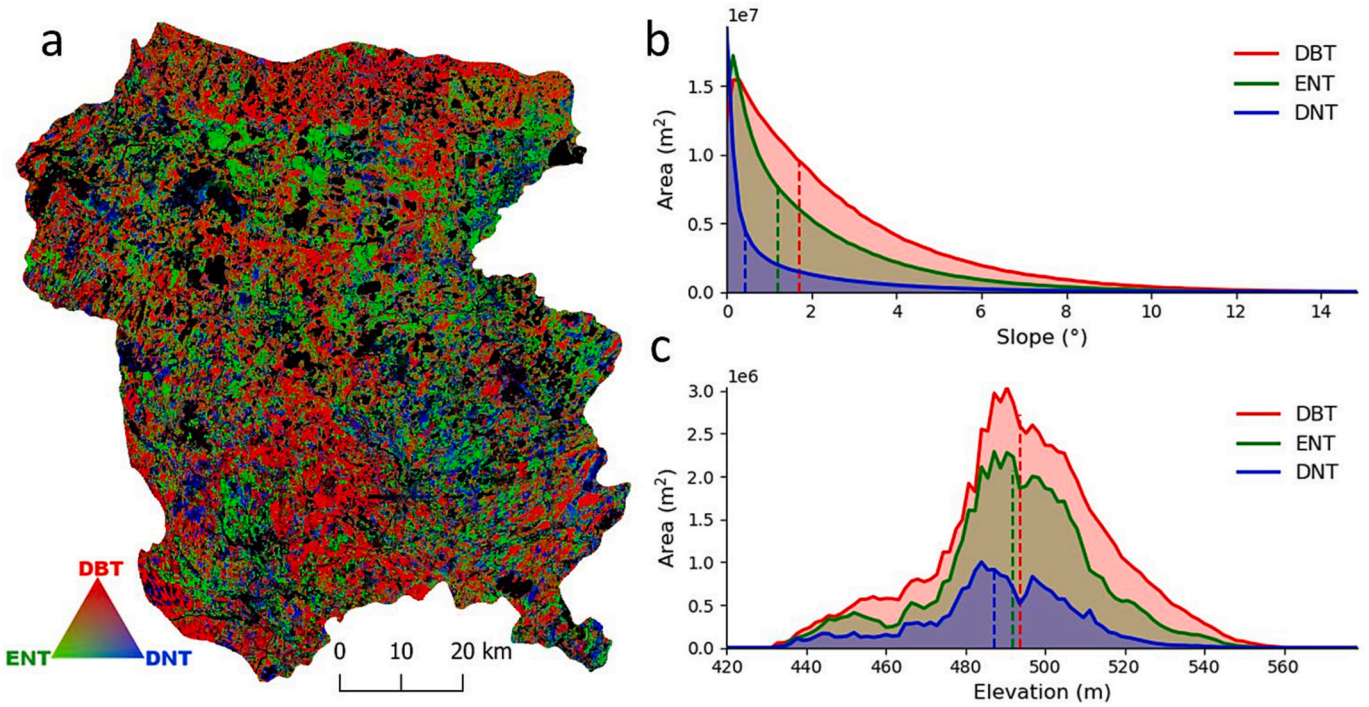

Fig. 7. Spatial and vertical distribution of TFT in the northern upland ecoregion. (a) Estimated fractions of DBT, ENT, and DNT, respectively. (c, d) Tree growing niches along the slope and elevation gradients. Dashed lines represent the median value of each corresponding TFT distribution.

comes with a cost, as it will bring certain features that show high sensitivity to ambient conditions (e.g., residual cloud/aerosol contamination, snow effect, topography effect) and results in a much lower signal-to-noise ratio (Gómez et al., 2016; Zhang et al., 2019). For example, the low accuracy of nonF type is likely due to the high within-class variability associated with diverse land materials and ambience noises across space and time, which is difficult to capture with the constructed endmember library. This high variability is evident in the PCA space of pure pixels, which shows that nonF has significantly larger within-class variability compared to other land classes of interest (Fig. 3a and b). The use of FDA tended to help suppress the impact associated with these ambient noises through feature dimension reduction, leading to improved TFT fractional mapping, especially for those TFTs with rare-to-subdominant abundance (i.e., DNT and nonF; Figs. 3–5).

Despite this effectiveness of FDA in handling signal variability of endmembers from diverse and heterogeneous landscapes, the selection of endmembers from representative locations is also critical as it leaded to marked accuracy difference between sites and TFTs (Fig. S6). Specifically, DBT that often presents at mountainous regions and its signals are affected by local topographic conditions, thus endmembers extracted from the CHEQ site exhibit lower representativeness to the other two sites (RMSE = 0.19 and 0.20 against 0.15). For the DNT, because it is strongly influenced by the background signal from diverse wetland habitats (water and moist soil) (Benninga et al., 2019), the DNT endmembers extracted from wetland site UNDE thus being less representative to the other two sites with lowest accuracy among TFTs (RMSE = 0.19 and 0.24 against 0.14). These results underscore the importance of explicitly accounting for environmental heterogeneity in the selection to improve the scalability of the model across larger and diverse landscapes.

Our validation approach differs from most previous unmixing studies in terms of both the benchmark data used (i.e., fraction maps across divergent landscapes) and the validation strategy employed (i.e., independent K-fold evaluation). Previous studies commonly used fraction validation datasets that only cover a small fraction of research regions, such as phenology camera (PhenoCam) imagery (Sousa and Davis, 2020) or manual interpretation/field survey plots (Bolyn et al., 2022; Nill et al., 2022; Okujeni et al., 2021), given the difficulty to generate finer-scale benchmark dataset covering large landscapes. Our benchmark data, which covers 392 km^2 and spans a distance of 100 km between sites, is crucial for evaluating the generalizability of the model across landscapes with diverse TFT compositions and high spatial heterogeneity. This provides an improved assessment of the model's predictive capabilities under different scenarios. Additionally, the independent K-fold accuracy assessment is vital for the non-biased validation of fraction estimations, but it was rarely used among the previous TFT fraction validation exercises. In this regard, our study provides a more rigorous and comparable accuracy assessment of our proposed F-SRTMA framework.

Our F-SRTMA framework embeds three independent and easy-to-implement modules (i.e., SRT feature reconstruction, spatial-guided endmember extraction, and FDA features) into the SMA framework, which implies that our modeling framework can be largely adapted to other novel endmember extraction/unmixing algorithms or future advanced remote sensing datasets. Specifically, our locally extracted endmembers with time-series features are tractable for any location or multi-year estimations. This is because the reconstructed SRT features in monthly format can counteract the influence of various observational dates across large landscapes and different years, in contrast to other time-series mixture analysis models that only use good-quality satellite imagery with varying acquisition dates across landscapes or years (Hemmerling et al., 2021; Okujeni et al., 2021; Wang et al., 2021). Moreover, the whole framework was developed on GEE, making it easy to be extended to other remote sensing datasets or locations.

4.3. Ecological implications

The derived fractional TFT compositions provide an important dataset for interpreting the processes underlying the regulation of ecosystem multi-functionality in this ecoregion. Previous studies have shown that the magnitude and directional change of understory

vegetation composition and density with climate change are largely mediated by the upper canopies of broadleaved vs. conifer TFTs due to their distinct canopy structures (Cook, 2015; Sonnier et al., 2020; Wiegmann and Waller, 2006). In addition, due to the fundamental differences in plant phenological and physiological characteristics among different TFTs, fractional TFT compositions improve understanding and modeling of their impacts on ecosystem phenology (Smith and Keenan, 2020), light/water use efficiency (Ahl et al., 2004; Murphy et al., 2022), as well as water/carbon flux seasonality (Krasnova et al., 2019; Mackay et al., 2002). Since these studies were mainly based on site/plot-level datasets, our ecoregion-wise TFT fraction map provides a way to scale up this site-level knowledge.

Furthermore, the generated dataset provides a unique opportunity to understand the overall picture of multifaceted TFT assemblages in the upland mixed forest ecoregion and to reveal proximate environmental drivers underlying the observed patterns (Fig. 7). Generally, DBT was found to be the dominant TFT in this ecoregion, while DNT was found to be the most fragmented across the entire ecoregion (NatureServe, 2009). The fractional TFT distribution along elevational gradients supports the topographic niche hypothesis that has often been hypothesized for explaining the biogeography of TFT distributions (Fig. 7b and c; Bai et al., 2015). The shared and separated elevational niches among different TFTs indicate that DNT (mostly fir (Abies spp.) and tamarack (Larix spp.)) are well mixed with the ENT (typically including pine (Pinus spp.) and spruce (Picea spp.)) in lowland floodplains (i.e., by lakes or wetlands), while DBT becomes dominant in elevated and steeper regions (Fig. 7b). Notably, our estimates of the area-based distribution of TFTs are closely related to local species-level observations that DNT mainly grows in warmer and wetter areas while DBT can survive in colder and drier environments (Mamet et al., 2019; Neves et al., 2021; Waller et al., 2013). The results reinforce the finding that the TFT mixture is notably evident in temperate regions, where TFT fractions often exhibit significant variations across environmental gradients. These variations can be attributed to a range of factors, including climatic and topographic conditions, as well as intricate complex interactions between vegetation, climate, topography, and disturbance histories (Echeverría-Londoño et al., 2018; Hansen et al., 2013; Swenson et al., 2012).

Our results demonstrate that subpixel-level fractions are more efficient than discrete classes for characterizing forest density and volume. They show a higher accuracy with airborne LiDAR-based canopy height results than the other two state-of-the-art forested products (Fig. 8). Forest fractions, including fractions of forest gaps and forest edges, can be used to infer the density/volume of the forest fragmentation level, an essential metric for studying forest multi-functionality, such as carbon cycling (Krasnova et al., 2019; Moore et al., 2016), forest mortality (Barton et al., 2017), drought and other stress responses (Gleason et al., 2017). However, this relevant information was not well depicted for the temperate mixed forest ecosystem because the size of canopy gaps among the sparse stands is often smaller than the area of a satellite image pixel, as shown in the examples in Fig. 8. The F-SRTMA framework for subpixel abundance mapping is thus advantageous for characterizing such fragmented forest compositions in both mixed and open-canopy forest ecosystems.

4.4. Limitation and future perspective

Our study has three main limitations, and further efforts could enhance TFT fractional mapping. First, relying on land cover data to determine TFT endmember types (step 2 in Section 2.3.2) may limit the approach's applicability in areas where land cover reference is unavailable. Furthermore, the accuracy of existing land cover maps may not always be sufficient for determining endmember types. The spatial-spectral-based refinement method, such as MEI used in this study, may only select one dominant type of pure pixel per kernel neighborhood, potentially leading to the loss of important endmembers in certain situations, especially the land type with small coverage (i.e., TFT with rare abundance). Thus, instead of relying solely on specific reference

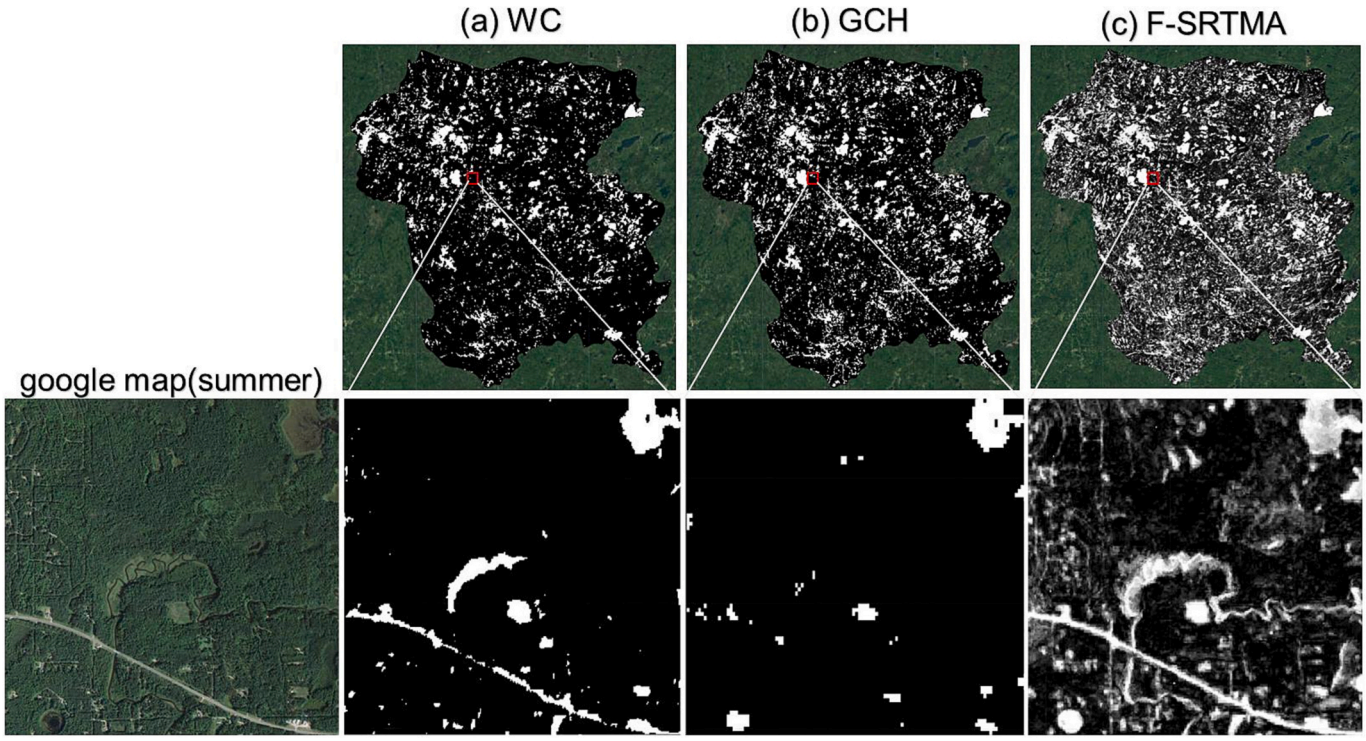

Fig. 8. Comparison of fraction and discrete classification maps in characterizing fragmented non-forest land cover. (a, b) Two state-of-the-art discrete non-forest maps. (c) F-SRTMA-based non-forest fraction map. Estimated fractions scaled from [0, 1], with white and black corresponding to 100% of the non-forest and forest classes, respectively.

maps, we suggest determining land cover automatically using empirical constraints, such as vegetation index-based thresholds (Wang et al., 2023), or doing it manually through visual interpretation (Nill et al., 2022; Ouyang et al., 2022; Schug et al., 2020). As more high-spatial resolution reference datasets are becoming available across continents, such as the IDtrees NIST NEON submeter airborne classification map (Weinstein et al., 2019), or forest in-situ survey datasets such as LUCAS (D'Andrimont et al., 2020) and SiDroForest (van Geffen et al., 2022), we anticipate that these restrictions can be alleviated in the future.

Second, the shallow penetration depth (around 5 cm) of Sentinel-1C-band data limits its sensitivity to tree structure detection (Ling et al., 2022), as we observed significant overlap between the conifers (ENT and DNT) endmembers of VV and VH bands (Fig. 2k and l). To address this issue, future studies are suggested to use longer wavelength bands of SAR data, such as L-band (with a wavelength of 15–30 cm) and P-band (with a wavelength of 30-100 cm). These longer wavelength bands offer a significantly enhanced ability to penetrate deeper into forest canopies and provide multi-layer structural information (Carreiras et al., 2017; Englhart et al., 2011). Ultimately, this could increase the signal-to-noise ratio of the extracted forest structure information (Li et al., 2019). Examples of suitable SAR data for this purpose include PALSAR (Rosenqvist et al., 2007) and BIOMASS(Sedehi et al., 2021).

Third, our proposed F-SRTMA framework exhibits high scalability and is designed for integration with various data sources or algorithms in the future. Although our study employed the F-SRTMA framework based on Sentinel −1 and − 2 imagery, it can be extended and scaled to accommodate different sensors, such as ALOS PALSAR, Landsat, and EnMAP (Brell et al., 2021; Rosenqvist et al., 2007). In this study, we utilized MESMA, an advanced model that only considers only linear mixture mechanisms. However, it is essential to acknowledge the presence of nonlinear multi-scattering effects in SAR data introduces significant uncertainty when using a linear mixture model, such as the one employed in our study, to assimilate RT features for TFT fraction mapping. This highlights the need for the development of more sophisticated models that can accurately represent this nonlinearity in future research. The open structure of the F-SRTMA framework enables the use of other state-of-the-art unmixing algorithms to model both linear and non-linear mixtures, such as machine learning regression-based unmixing models (Okujeni et al., 2017; Senf et al., 2020) and spectral-spatial deep learning models (Bolyn et al., 2022).

5. Conclusion

Fractional tree functional type (TFT) composition is an important metric that is tightly related to the multi-functionality of temperate mixed forest ecosystems. In this study, we developed an F-SRTMA framework to enhance TFT fraction mapping using time-series Sentinel −1 and − 2 data, aiming to advance the characterization of high spatial TFT heterogeneity in temperate mixed forest ecotones. The framework includes four steps: reconstructing standardized SRT features based on time-series Sentinel-1 and -2 imagery (step 1), identifying candidate endmembers using a spatial-guided endmember selection method (step 2), optimizing the endmember space-time variability with FDA (step 3), and estimating the endmember abundances per pixel from a MESMA model (step 4). Our proposed F-SRTMA approach was rigorously evaluated and exhibited higher accuracy (RMSE = 0.150, r^2 = 0.754) compared to recent advanced STMA (RMSE = 0.180, r^2 = 0.649) and conventional SMA (RMSE = 0.222, r^2 = 0.550). Moreover, the inclusion of radar time-series improved generalizability across sites (RMSE = 0.222 vs. 0.207 for STMA and SRTMA), and the integration of FDA (F-SRTMA) achieved more consistent and significantly higher cross-site accuracy (RMSE = 0.164). Our work demonstrates the advantages of integrating spectral and radar time-series signals for improved unmixing modeling, which holds significant theoretical implications. Additionally, our proposed F-SRTMA framework provides an effective way to utilize spectral and radar time series for TFT fractional mapping, offering new avenues for refining the fusion of spectral and radar information.

The framework, built on the GEE platform, facilitates the detection of fractional TFT composition variations across diverse landscapes on an ecoregion level, providing an essential dataset to support subsequent, more complex ecological studies of this system. We contend that our framework could be equally suitable for mapping other important metrics, such as urban and vegetation fractions, and could be scaled for different time-series spectral and radar remote sensing datasets and integrated with various unmixing algorithms.

CRediT authorship contribution statement

Ziyu Lin: Writing – review & editing, Writing – original draft, Visualization, Validation, Software, Resources, Project administration, Methodology, Investigation, Formal analysis, Data curation, Conceptualization. **K.H. Cheng:** Writing – review & editing. **Dedi Yang:** Writing – review & editing. **Fei Xu:** Writing – review & editing. **Guangqin Song:** Writing – review & editing. **Ran Meng:** Writing – review & editing. **Jing Wang:** Writing – review & editing. **Xiaolin Zhu:** Writing – review & editing. **Michael Ng:** Writing – review & editing. **Jin Wu:** Writing – review & editing, Supervision.

Declaration of competing interest

The authors declare that they have no known competing financial interests or personal relationships that could have appeared to influence the work reported in this paper.

Data availability

Data will be made available on request.

Acknowledgements

We would like to thank the editors and two reviewers for providing valuable suggestions and comments, which are greatly helpful in improving the quality of this work. The work was primarily supported by the National Natural Science Foundation of China (#31922090), Hong Kong Research Grant Council General Research Fund (#17316622 and #17305321) and Collaborative Research Fund (#C5062-21GF), the HKU Seed Funding for Basic Research (2021115931), the HKU Seed Funding for Strategic Interdisciplinary Research Scheme, the Hung Ying Physical Science Research Fund 2021-22, and the Innovation and Technology Fund (funding support to State Key Laboratories in Hong Kong of Agrobiotechnology) of the HKSAR, China. RM was supported by the Fundamental Research Funds for the Central Universities, Beijing, China (Grant Nos. 2662022ZHYJ002; 2662022JC006). DY was supported by the United States Department of Energy contract No. DE-SC0012704 to Brookhaven National Laboratory and NASA's Future Investigators in NASA Earth and Space Science and Technology (FINESST) Grant 80NSSC22K1296. MNg is funded by HKRGC GRF 12300519, 17201020 and 17300021, HKRGC CRF C1013-21GF and C7004-21GF, and Joint NSFC and RGC N-HKU769/21.

All the relevant processes and statistics were coded in JavaScript based on the API of Earth Engine, and Python 3.9 (Python Software Foundation, https://www.python.org/) and will be shared on GitHub (https://github.com/) upon acceptance.

Appendix A. Supplementary data

Supplementary data to this article can be found online at https://doi.org/10.1016/j.rse.2024.114026.

References

Adams, J.B., Gillespie, A.R., 2006. Remote Sensing of Landscapes with Spectral Images: A Physical Modeling Approach, 1st ed. Cambridge University Press. https://doi.org/10.1017/CBO9780511617195.

Ahl, D.E., Gower, S.T., Mackay, D.S., Burrows, S.N., Norman, J.M., Diak, G.R., 2004. Heterogeneity of light use efficiency in a northern Wisconsin forest: implications for modeling net primary production with remote sensing. Remote Sens. Environ. 93, 168–178. https://doi.org/10.1016/j.rse.2004.07.003.

Anderegg, W.R.L., Konings, A.G., Trugman, A.T., Yu, K., Bowling, D.R., Gabbitas, R., Karp, D.S., Pacala, S., Sperry, J.S., Sulman, B.N., Zenes, N., 2018. Hydraulic diversity of forests regulates ecosystem resilience during drought. Nature 561, 538–541. https://doi.org/10.1038/s41586-018-0539-7.

Arii, M., Yamada, H., Kojima, S., Ohki, M., 2019. Review of the comprehensive SAR approach to identify scattering mechanisms of radar backscatter from vegetated terrain. Electronics 8, 1098. https://doi.org/10.3390/electronics8101098.

Bai, K., He, C., Wan, X., Jiang, D., 2015. Leaf economics of evergreen and deciduous tree species along an elevational gradient in a subtropical mountain. AoB PLANTS 7, plv064. https://doi.org/10.1093/aobpla/plv064.

Barton, I., Király, G., Czimber, K., Hollaus, M., Pfeifer, N., 2017. Treefall gap mapping using Sentinel-2 images. Forests 8, 426. https://doi.org/10.3390/f8110426.

Benninga, H.-J.F., van der Velde, R., Su, Z., 2019. Impacts of radiometric uncertainty and weather-related surface conditions on soil moisture retrievals with Sentinel-1. Remote Sens. 11, 2025. https://doi.org/10.3390/rs11172025.

Bolyn, C., Lejeune, P., Michez, A., Latte, N., 2022. Mapping tree species proportions from satellite imagery using spectral–spatial deep learning. Remote Sens. Environ. 280, 113205 https://doi.org/10.1016/j.rse.2022.113205.

Box, E.O., Fujiwara, K. (Eds.), 2015. Warm-Temperate Deciduous Forests around the Northern Hemisphere, Geobotany Studies. Springer International Publishing, Cham. https://doi.org/10.1007/978-3-319-01261-2.

Brell, M., Guanter, L., Segl, K., Scheffler, D., Bohn, N., Bracher, A., Soppa, M.A., Foerster, S., Storch, T., Bachmann, M., Chabrillat, S., 2021. The EnMAP satellite –data product validation activities. In: 2021 11th Workshop on Hyperspectral Imaging and Signal Processing: Evolution in Remote Sensing (WHISPERS). Presented at the 2021 11th Workshop on Hyperspectral Imaging and Signal Processing: Evolution in Remote Sensing (WHISPERS), pp. 1–5. https://doi.org/10.1109/WHISPERS52202.2021.9484000.

Bro, R., Jong, S.D., 1997. A fast non-negativity-constrained least squares algorithm. J. Chemom. 11, 10.

Carlson, T.N., Ripley, D.A., 1997. On the relation between NDVI, fractional vegetation cover, and leaf area index. Remote Sens. Environ. 62, 241–252. https://doi.org/10.1016/S0034-4257(97)00104-1.

Carreiras, J.M.B., Quegan, S., Le Toan, T., Ho Tong Minh, D., Saatchi, S.S., Carvalhais, N., Reichstein, M., Scipal, K., 2017. Coverage of high biomass forests by the ESA BIOMASS mission under defense restrictions. Remote Sens. Environ. 196, 154–162. https://doi.org/10.1016/j.rse.2017.05.003.

Chen, J., Jönsson, Per, Tamura, M., Gu, Z., Matsushita, B., Eklundh, L., 2004. A simple method for reconstructing a high-quality NDVI time-series data set based on the Savitzky–Golay filter. Remote Sens. Environ. 91, 332–344. https://doi.org/10.1016/j.rse.2004.03.014.

Chen, X., Chen, J., Jia, X., Somers, B., Wu, J., Coppin, P., 2011. A quantitative analysis of virtual Endmembers' increased impact on the collinearity effect in spectral Unmixing. IEEE Trans. Geosci. Remote Sens. 49, 2945–2956. https://doi.org/10.1109/TGRS.2011.2121073.

Claverie, M., Ju, J., Masek, J.G., Dungan, J.L., Vermote, E.F., Roger, J.-C., Skakun, S.V., Justice, C., 2018. The harmonized Landsat and Sentinel-2 surface reflectance data set. Remote Sens. Environ. 219, 145–161. https://doi.org/10.1016/j.rse.2018.09.002.

Cohen, W.B., Spies, T.A., Bradshaw, G.A., 1990. Semivariograms of digital imagery for analysis of conifer canopy structure. Remote Sens. Environ. 34, 167–178. https://doi.org/10.1016/0034-4257(90)90066-U.

Cook, J.E., 2015. Structural effects on understory attributes in second-growth forests of northern Wisconsin, USA. For. Ecol. Manag. 347, 188–199. https://doi.org/10.1016/j.foreco.2015.03.027.

Cooley, S.S., Fisher, J.B., Goldsmith, G.R., 2022. Convergence in water use efficiency within plant functional types across contrasting climates. Nat. Plants 8, 341–345. https://doi.org/10.1038/s41477-022-01131-z.

D'Andrimont, R., Yordanov, M., Martinez-Sanchez, L., Eiselt, B., Palmieri, A., Dominici, P., Gallego, J., Reuter, H.I., Joebges, C., Lemoine, G., Van Der Velde, M., 2020. Harmonised LUCAS in-situ land cover and use database for field surveys from 2006 to 2018 in the European Union. Sci. Data 7. https://doi.org/10.1038/s41597-020-00675-z.

Degerickx, J., Roberts, D.A., Somers, B., 2019. Enhancing the performance of multiple endmember spectral mixture analysis (MESMA) for urban land cover mapping using airborne lidar data and band selection. Remote Sens. Environ. 221, 260–273. https://doi.org/10.1016/j.rse.2018.11.026.

Díaz, S., Cabido, M., 2001. Vive la différence: plant functional diversity matters to ecosystem processes. Trends Ecol. Evol. 16, 646–655. https://doi.org/10.1016/S0169-5347(01)02283-2.

Dostálová, A., Wagner, W., Milenković, M., Hollaus, M., 2018. Annual seasonality in Sentinel-1 signal for forest mapping and forest type classification. Int. J. Remote Sens. 39, 7738–7760. https://doi.org/10.1080/01431161.2018.1479788.

Echeverría-Londoño, S., Enquist, B.J., Neves, D.M., Violle, C., Boyle, B., Kraft, N.J.B., Maitner, B.S., McGill, B., Peet, R.K., Sandel, B., Smith, S.A., Svenning, J.-C., Wiser, S. K., Kerkhoff, A.J., 2018. Plant functional diversity and the biogeography of biomes in north and South America. Front. Ecol. Evol. 6, 219. https://doi.org/10.3389/fevo.2018.00219.

Englhart, S., Keuck, V., Siegert, F., 2011. Aboveground biomass retrieval in tropical forests — the potential of combined X- and L-band SAR data use. Remote Sens. Environ. 115, 1260–1271. https://doi.org/10.1016/j.rse.2011.01.008.

Espelta, J.M., Cruz-Alonso, V., Alfaro-Sánchez, R., Hampe, A., Messier, C., Pino, J., 2020. Functional diversity enhances tree growth and reduces herbivory damage in secondary broadleaf forests, but does not influence resilience to drought. J. Appl. Ecol. 57, 2362–2372. https://doi.org/10.1111/1365-2664.13728.

Feng, Z., Zheng, X., Li, L., Li, B., Chen, S., Guo, T., Wang, X., Jiang, T., Li, Xiaojie, Li, Xiaofeng, 2021. Dynamic cosine method for normalizing incidence angle effect on C-band radar backscattering coefficient for maize canopies based on NDVI. Remote Sens. 13, 2856. https://doi.org/10.3390/rs13152856.

Ferguson, J.E., Gunn, G.E., 2022. Polarimetric decomposition of microwave-band freshwater ice SAR data: review, analysis, and future directions. Remote Sens. Environ. 280, 113176 https://doi.org/10.1016/j.rse.2022.113176.

Flores-Anderson, A.I., Herndon, K.E., Thapa, R.B., Cherrington, E., 2019. The SAR Handbook: Comprehensive Methodologies for Forest Monitoring and Biomass Estimation. https://doi.org/10.25966/nr2c-s697.

Freeman, A., Durden, S.L., 1998. A three-component scattering model for polarimetric SAR data. IEEE Trans. Geosci. Remote Sens. 36, 963–973. https://doi.org/10.1109/36.673687.

Gao, L., Wang, X., Johnson, B.A., Tian, Q., Wang, Y., Verrelst, J., Mu, X., Gu, X., 2020. Remote sensing algorithms for estimation of fractional vegetation cover using pure vegetation index values: a review. ISPRS J. Photogramm. Remote Sens. 159, 364–377. https://doi.org/10.1016/j.isprsjprs.2019.11.018.

Gascoin, S., Grizonnet, M., Bouchet, M., Salgues, G., Hagolle, O., 2019. Theia snow collection: high-resolution operational snow cover maps from Sentinel-2 and Landsat-8 data. Earth Syst. Sci. Data 11, 493–514. https://doi.org/10.5194/essd-11-493-2019.

Giordano, S., Mercier, G., Rudant, J.-P., 2018. Unmixing Polarimetric radar images based on land cover type identified by higher resolution optical data before target decomposition: application to Forest and bare soil. IEEE Trans. Geosci. Remote Sens. 56, 5850–5862. https://doi.org/10.1109/tgrs.2018.2827258.

Gleason, K.E., Bradford, J.B., Bottero, A., D'Amato, A.W., Fraver, S., Palik, B.J., Battaglia, M.A., Iverson, L., Kenefic, L., Kern, C.C., 2017. Competition amplifies drought stress in forests across broad climatic and compositional gradients. Ecosphere 8, e01849. https://doi.org/10.1002/ecs2.1849.

Gómez, C., White, J.C., Wulder, M.A., 2016. Optical remotely sensed time series data for land cover classification: a review. ISPRS J. Photogramm. Remote Sens. 116, 55–72. https://doi.org/10.1016/j.isprsjprs.2016.03.008.

Gorelick, N., Hancher, M., Dixon, M., Ilyushchenko, S., Thau, D., Moore, R., 2017. Google Earth engine: planetary-scale geospatial analysis for everyone. Remote Sens. Environ. 202, 18–27. https://doi.org/10.1016/j.rse.2017.06.031.

Han, X., Xu, Y., Huang, J., Zang, R., 2022. Species diversity regulates ecological strategy spectra of Forest vegetation across different climatic zones. Front. Plant Sci. 13.

Hansen, M.C., Potapov, P.V., Moore, R., Hancher, M., Turubanova, S.A., Tyukavina, A., Thau, D., Stehman, S.V., Goetz, S.J., Loveland, T.R., Kommareddy, A., Egorov, A., Chini, L., Justice, C.O., Townshend, J.R.G., 2013. High-resolution global maps of 21st-century Forest cover change. Science 342, 850–853. https://doi.org/10.1126/science.1244693.

Heinz, D.C., Chein-I-Chang, 2001. Fully constrained least squares linear spectral mixture analysis method for material quantification in hyperspectral imagery. IEEE Trans. Geosci. Remote Sens. 39, 529–545. https://doi.org/10.1109/36.911111.

Hemmerling, J., Pflugmacher, D., Hostert, P., 2021. Mapping temperate forest tree species using dense Sentinel-2 time series. Remote Sens. Environ. 267, 112743 https://doi.org/10.1016/j.rse.2021.112743.

Hillebrand, F.L., Bremer, U.F., de Freitas, M.W.D., Costi, J., Mendes Júnior, C.W., Arigony-Neto, J., Simões, J.C., 2022. Spectral linear mixing model applied to data from passive microwave radiometers for sea ice mapping in the Antarctic peninsula. Geocarto Int. 37, 3141–3166. https://doi.org/10.1080/10106049.2020.1856194.

Jin, J., Wang, B., Zhang, L., 2010. A novel approach based on Fisher discriminant null space for decomposition of mixed pixels in hyperspectral imagery. IEEE Geosci. Remote Sens. Lett. 7, 699–703. https://doi.org/10.1109/lgrs.2010.2046134.

Jolliffe, I., 2011. Principal component analysis. In: Lovric, M. (Ed.), International Encyclopedia of Statistical Science. Springer Berlin Heidelberg, Berlin, Heidelberg, pp. 1094–1096. https://doi.org/10.1007/978-3-642-04898-2_455.

Joshi, N.P., Mitchard, E.T.A., Schumacher, J., Johannsen, V.K., Saatchi, S., Fensholt, R., 2015. L-band SAR backscatter related to Forest cover, height and aboveground biomass at multiple spatial scales across Denmark. Remote Sens. 7, 4442–4472. https://doi.org/10.3390/rs70404442.

Jung, M., Arnell, A., de Lamo, X., García-Rangel, S., Lewis, M., Mark, J., Merow, C., Miles, L., Ondo, I., Pironon, S., Ravilious, C., Rivers, M., Schepaschenko, D., Tallowin, O., van Soesbergen, A., Govaerts, R., Boyle, B.L., Enquist, B.J., Feng, X., Gallagher, R., Maitner, B., Meiri, S., Mulligan, M., Ofer, G., Roll, U., Hanson, J.O., Jetz, W., Di Marco, M., McGowan, J., Rinnan, D.S., Sachs, J.D., Lesiv, M., Adams, V. M., Andrew, S.C., Burger, J.R., Hannah, L., Marquet, P.A., McCarthy, J.K., Morueta-Holme, N., Newman, E.A., Park, D.S., Roehrdanz, P.R., Svenning, J.-C., Violle, C., Wieringa, J.J., Wynne, G., Fritz, S., Strassburg, B.B.N., Obersteiner, M., Kapos, V., Burgess, N., Schmidt-Traub, G., Visconti, P., 2021. Areas of global importance for conserving terrestrial biodiversity, carbon and water. Nat. Ecol. Evol. 5, 1499–1509. https://doi.org/10.1038/s41559-021-01528-7.

Kampe, T.U., Johnson, B.R., Kuester, M.A., Keller, M., 2010. NEON: the first continental-scale ecological observatory with airborne remote sensing of vegetation canopy biochemistry and structure. JARS 4, 043510. https://doi.org/10.1117/1.3361375.

Krasnova, A., Kukumägi, M., Mander, Ü., Torga, R., Krasnov, D., Noe, S.M., Ostonen, I., Püttsepp, Ü., Killian, H., Uri, V., Lõhmus, K., Sõber, J., Soosaar, K., 2019. Carbon exchange in a hemiboreal mixed forest in relation to tree species composition. Agric. For. Meteorol. 275, 11–23. https://doi.org/10.1016/j.agrformet.2019.05.007.

Li, X., Liu, Y., Xu, W., Huang, P., Fu, W., 2019. Forest canopy volume density index inversion method using polarization decomposition. In: Presented at the 2019 Photonics & Electromagnetics Research Symposium - Fall (PIERS - Fall). IEEE. https://doi.org/10.1109/piers-fall48861.2019.9021425.

Ling, Y., Teng, S., Liu, C., Dash, J., Morris, H., Pastor-Guzman, J., 2022. Assessing the accuracy of Forest Phenological extraction from Sentinel-1 C-band backscatter measurements in deciduous and coniferous forests. Remote Sens. 14, 674. https://doi.org/10.3390/rs14030674.

Liu, M., Yang, W., Chen, J., Chen, X., 2017. An orthogonal Fisher transformation-based Unmixing method toward estimating fractional vegetation cover in semiarid areas. IEEE Geosci. Remote Sens. Lett. 14, 449–453. https://doi.org/10.1109/lgrs.2017.2648863.

Mackay, D.S., Ahl, D.E., Ewers, B.E., Gower, S.T., Burrows, S.N., Samanta, S., Davis, K.J., 2002. Effects of aggregated classifications of forest composition on estimates of evapotranspiration in a northern Wisconsin forest. Glob. Chang. Biol. 8, 1253–1265. https://doi.org/10.1046/j.1365-2486.2002.00554.x.

Malenovský, Z., Rott, H., Cihlar, J., Schaepman, M.E., García-Santos, G., Fernandes, R., Berger, M., 2012. Sentinels for science: potential of Sentinel-1, −2, and −3 missions for scientific observations of ocean, cryosphere, and land. Remote Sens. Environ. Sentin. Missions New Opportunities Sci. 120, 91–101. https://doi.org/10.1016/j.rse.2011.09.026.

Mamet, S.D., Brown, C.D., Trant, A.J., Laroque, C.P., 2019. Shifting globalLarixdistributions: northern expansion and southern retraction as species respond to changing climate. J. Biogeogr. 46, 30–44. https://doi.org/10.1111/jbi.13465.

McFeeters, S.K., 1996. The use of the normalized difference water index (NDWI) in the delineation of open water features. Int. J. Remote Sens. 17, 1425–1432. https://doi.org/10.1080/01431169608948714.

Mei, S., He, M., Wang, Z., Feng, D., 2010. Spatial purity based endmember extraction for spectral mixture analysis. IEEE Trans. Geosci. Remote Sens. 48, 3434–3445. https://doi.org/10.1109/tgrs.2010.2046671.

Mendes, F., Baron, D., Gerold, G., Liesenberg, V., Erasmi, S., 2019. Optical and SAR remote sensing synergism for mapping vegetation types in the endangered Cerrado/Amazon ecotone of Nova Mutum—Mato Grosso. Remote Sens. 11, 1161. https://doi.org/10.3390/rs11101161.

Moore, C.E., Beringer, J., Evans, B., Hutley, L.B., Mchugh, I., Tapper, N.J., 2016. The contribution of trees and grasses to productivity of an Australian tropical savanna. Biogeosciences 13, 2387–2403. https://doi.org/10.5194/bg-13-2387-2016.

Mullissa, A., Vollrath, A., Odongo-Braun, C., Slagter, B., Balling, J., Gou, Y., Gorelick, N., Reiche, J., 2021. Sentinel-1 SAR backscatter analysis ready data preparation in Google earth engine. Remote Sens. 13, 1954. https://doi.org/10.3390/rs13101954.

Murphy, B.A., May, J.A., Butterworth, B.J., Andresen, C.G., Desai, A.R., 2022. Unraveling Forest complexity: resource use efficiency, disturbance, and the structure-function relationship. J. Geophys. Res. Biogeosci. 127, e2021JG006748 https://doi.org/10.1029/2021JG006748.

NatureServe, 2009. NatureServe Explorer: An online encyclopedia of life [web application]. Version 7.1. NatureServe Arlington, Virginia.

Neves, D.M., Kerkhoff, A.J., Echeverría-Londoño, S., Merow, C., Morueta-Holme, N., Peet, R.K., Sandel, B., Svenning, J.-C., Wiser, S.K., Enquist, B.J., 2021. The adaptive challenge of extreme conditions shapes evolutionary diversity of plant assemblages at continental scales. Proc. Natl. Acad. Sci. USA 118, e2021132118. https://doi.org/10.1073/pnas.2021132118.

Nill, L., Grünberg, I., Ullmann, T., 2022. Arctic shrub expansion revealed by Landsat-derived multitemporal vegetation cover fractions in the Western Canadian Arctic. Remote Sens. Environ. 281, 113228 https://doi.org/10.1016/j.rse.2022.113228.

Okada, T., Tomita, S., 1985. An optimal orthonormal system for discriminant analysis. Pattern Recogn. 18, 139–144. https://doi.org/10.1016/0031-3203(85)90037-8.

Okujeni, A., van der Linden, S., Suess, S., Hostert, P., 2017. Ensemble learning from synthetically mixed training data for quantifying urban land cover with support vector regression. IEEE J. Select. Top. Appl. Earth Observ. Remote Sens. 10, 1640–1650. https://doi.org/10.1109/JSTARS.2016.2634859.

Okujeni, A., Jänicke, C., Cooper, S., Frantz, D., Hostert, P., Clark, M., Segl, K., van der Linden, S., 2021. Multi-season unmixing of vegetation class fractions across diverse Californian ecoregions using simulated spaceborne imaging spectroscopy data. Remote Sens. Environ. 264, 112558 https://doi.org/10.1016/j.rse.2021.112558.

Otsu, N., 1979. A threshold selection method from gray-level histograms. IEEE Trans. Syst. Man Cybern. 9, 62–66. https://doi.org/10.1109/TSMC.1979.4310076.

Ouyang, L., Wu, C., Li, J., Liu, Y., Wang, M., Han, J., Song, C., Yu, Q., Haase, D., 2022. Mapping impervious surface using phenology-integrated and fisher transformed linear spectral mixture analysis. Remote Sens. https://doi.org/10.3390/rs14071673.

Parida, B.R., Mandal, S.P., 2020. Polarimetric decomposition methods for LULC mapping using ALOS L-band PolSAR data in Western parts of Mizoram, Northeast India. SN Appl. Sci. 2 https://doi.org/10.1007/s42452-020-2866-1.

Plaza, A., Martinez, P., Perez, R., Plaza, J., 2002. Spatial/spectral endmember extraction by multidimensional morphological operations. IEEE Trans. Geosci. Remote Sens. 40, 2025–2041. https://doi.org/10.1109/tgrs.2002.802494.

Potapov, P., Li, X., Hernandez-Serna, A., Tyukavina, A., Hansen, M.C., Kommareddy, A., Pickens, A., Turubanova, S., Tang, H., Silva, C.E., Armston, J., Dubayah, R., Blair, J.B., Hofton, M., 2021. Mapping global forest canopy height through integration of GEDI and Landsat data. Remote Sens. Environ. 253, 112165 https://doi.org/10.1016/j.rse.2020.112165.

Poulter, B., Macbean, N., Hartley, A., Khlystova, I., Arino, O., Betts, R., Bontemps, S., Boettcher, M., Brockmann, C., Defourny, P., Hagemann, S., Herold, M., Kirches, G., Lamarche, C., Lederer, D., Ottlé, C., Peters, M., Peylin, P., 2015. Plant functional type classification for earth system models: results from the European Space Agency's land cover climate change initiative. Geosci. Model Dev. 8, 2315–2328. https://doi.org/10.5194/gmd-8-2315-2015.

Powell, R.L., Roberts, D.A., Dennison, P.E., Hess, L.L., 2007. Sub-pixel mapping of urban land cover using multiple endmember spectral mixture analysis: Manaus, Brazil. Remote Sens. Environ. 106, 253–267. https://doi.org/10.1016/j.rse.2006.09.005.

Quintano, C., Fernández-Manso, A., Shimabukuro, Y.E., Pereira, G., 2012. Spectral unmixing. Int. J. Remote Sens. 33, 5307–5340. https://doi.org/10.1080/01431161.2012.661095.

Reiche, J., Hamunyela, E., Verbesselt, J., Hoekman, D., Herold, M., 2018. Improving near-real time deforestation monitoring in tropical dry forests by combining dense Sentinel-1 time series with Landsat and ALOS-2 PALSAR-2. Remote Sens. Environ. 204, 147–161. https://doi.org/10.1016/j.rse.2017.10.034.

Roberts, D.A., Gardner, M., Church, R., Ustin, S., Scheer, G., Green, R.O., 1998. Mapping chaparral in the Santa Monica Mountains using multiple endmember spectral mixture models. Remote Sens. Environ. 65, 267–279. https://doi.org/10.1016/S0034-4257(98)00037-6.

Roger, R.E., 1996. Principal components transform with simple, automatic noise adjustment. Int. J. Remote Sens. 17, 2719–2727. https://doi.org/10.1080/01431169608949102.

Rosenqvist, A., Shimada, M., Ito, N., Watanabe, M., 2007. ALOS PALSAR: a pathfinder Mission for global-scale monitoring of the environment. IEEE Trans. Geosci. Remote Sens. 45, 3307–3316. https://doi.org/10.1109/TGRS.2007.901027.

Roth, K.L., Dennison, P.E., Roberts, D.A., 2012. Comparing endmember selection techniques for accurate mapping of plant species and land cover using imaging spectrometer data. Remote Sens. Environ. 14.

Sabol, D.E., Adams, J.B., Smith, M.O., 1992. Quantitative subpixel spectral detection of targets in multispectral images. J. Geophys. Res. Planets 97, 2659–2672. https://doi.org/10.1029/91je03117.

Schmullius, C.C., Evans, D.L., 1997. Review article synthetic aperture radar (SAR) frequency and polarization requirements for applications in ecology, geology, hydrology, and oceanography: a tabular status quo after SIR-C/X-SAR. Int. J. Remote Sens. 18, 2713–2722. https://doi.org/10.1080/014311697217297.

Schubert, A., Miranda, N., Geudtner, D., Small, D., 2017. Sentinel-1A/B combined product geolocation accuracy. Remote Sens. 9, 607. https://doi.org/10.3390/rs9060607.

Schug, F., Frantz, D., Okujeni, A., van der Linden, S., Hostert, P., 2020. Mapping urban-rural gradients of settlements and vegetation at national scale using Sentinel-2 spectral-temporal metrics and regression-based unmixing with synthetic training data. Remote Sens. Environ. 246, 111810 https://doi.org/10.1016/j.rse.2020.111810.

Sedehi, M., Carbone, A., Imbembo, E., Heliere, F., Rommen, B., Fehringer, M., Scipal, K., Leanza, A., Simon, T., Willemsen, P., 2021. Biomass-a fully polarimetric P-band SAR ESA mission. In: EUSAR 2021; 13th European Conference on Synthetic Aperture Radar. VDE, pp. 1–5.

Senf, C., Laštovička, J., Okujeni, A., Heurich, M., van der Linden, S., 2020. A generalized regression-based unmixing model for mapping forest cover fractions throughout three decades of Landsat data. Remote Sens. Environ. 240, 111691 https://doi.org/10.1016/j.rse.2020.111691.

Settle, J.J., Drake, N.A., 1993. Linear mixing and the estimation of ground cover proportions. Int. J. Remote Sens. 14, 1159–1177. https://doi.org/10.1080/01431169308904402.

Shi, C., Wang, L., 2014. Incorporating spatial information in spectral unmixing: a review. Remote Sens. Environ. 149, 70–87. https://doi.org/10.1016/j.rse.2014.03.034.

Shimabukuro, Y.E., Smith, J.A., 1991. The least-squares mixing models to generate fraction images derived from remote sensing multispectral data. IEEE Trans. Geosci. Remote Sens. 29, 16–20. https://doi.org/10.1109/36.103288.

Singh, G., Malik, R., Mohanty, S., Rathore, V.S., Yamada, K., Umemura, M., Yamaguchi, Y., 2019. Seven-component scattering power decomposition of POLSAR coherency matrix. IEEE Trans. Geosci. Remote Sens. 57, 8371–8382. https://doi.org/10.1109/tgrs.2019.2920762.

Smith, N.G., Keenan, T.F., 2020. Mechanisms underlying leaf photosynthetic acclimation to warming and elevated CO 2 as inferred from least-cost optimality theory. Glob. Chang. Biol. 26, 5202–5216. https://doi.org/10.1111/gcb.15212.

Somers, B., Asner, G.P., Tits, L., Coppin, P., 2011. Endmember variability in spectral mixture analysis: a review. Remote Sens. Environ. 115, 1603–1616. https://doi.org/10.1016/j.rse.2011.03.003.

Sonnier, G., Johnson, S.E., Waller, D.M., 2020. Fragmentation reduces the importance of niche-based factors relative to dispersal traits in structuring temperate forest understories. J. Veg. Sci. 31, 75–83. https://doi.org/10.1111/jvs.12824.

Sousa, D., Davis, F.W., 2020. Scalable mapping and monitoring of Mediterranean-climate oak landscapes with temporal mixture models. Remote Sens. Environ. 247, 111937 https://doi.org/10.1016/j.rse.2020.111937.

Swenson, N.G., Enquist, B.J., Pither, J., Kerkhoff, A.J., Boyle, B., Weiser, M.D., Elser, J.J., Fagan, W.F., Forero-Montaña, J., Fyllas, N., Kraft, N.J.B., Lake, J.K., Moles, A.T., Patiño, S., Phillips, O.L., Price, C.A., Reich, P.B., Quesada, C.A., Stegen, J.C., Valencia, R., Wright, I.J., Wright, S.J., Andelman, S., Jørgensen, P.M., Lacher Jr., T.E., Monteagudo, A., Núñez-Vargas, M.P., Vasquez-Martínez, R., Nolting, K.M., 2012. The biogeography and filtering of woody plant functional diversity in North and South America: functional trait biogeography. Glob. Ecol. Biogeogr. 21, 798–808. https://doi.org/10.1111/j.1466-8238.2011.00727.x.

Tanase, M.A., Villard, L., Pitar, Diana, Apostol, B., Petrila, M., Chivulescu, S., Leca, S., Borlaf-Mena, I., Pascu, I.-S., Dobre, A.-C., Pitar, Daniel, Guiman, G., Lorent, A.,

Anghelus, C., Ciceu, A., Nedea, G., Stanculeanu, R., Popescu, F., Aponte, C., Badea, O., 2019. Synthetic aperture radar sensitivity to forest changes: a simulations-based study for the Romanian forests. Sci. Total Environ. 689, 1104–1114. https://doi.org/10.1016/j.scitotenv.2019.06.494.

Tian, D., Wang, L., 2022. Subpixel melt index in the Antarctic peninsula using spatially constrained linear Unmixing from time series satellite passive microwave images. IEEE Trans. Geosci. Remote Sens. 60, 1–9. https://doi.org/10.1109/tgrs.2020.3043330.

Ustin, S.L., Gamon, J.A., 2010. Remote sensing of plant functional types. New Phytol. 186, 795–816. https://doi.org/10.1111/j.1469-8137.2010.03284.x.

Van Cleemput, E., Helsen, K., Feilhauer, H., Honnay, O., Somers, B., 2021. Spectrally defined plant functional types adequately capture multidimensional trait variation in herbaceous communities. Ecol. Indic. 120, 106970 https://doi.org/10.1016/j.ecolind.2020.106970.

Van Der Plas, F., Manning, P., Allan, E., Scherer-Lorenzen, M., Verheyen, K., Wirth, C., Zavala, M.A., Hector, A., Ampoorter, E., Baeten, L., Barbaro, L., Bauhus, J., Benavides, R., Benneter, A., Berthold, F., Bonal, D., Bouriaud, O., Bruelheide, H., Bussotti, F., Carnol, M., Castagneyrol, B., Charbonnier, Y., Coomes, D., Coppi, A., Bastias, C.C., Muhie Dawud, S., De Wandeler, H., Domisch, T., Finér, L., Gessler, A., Granier, A., Grossiord, C., Guyot, V., Hättenschwiler, S., Jactel, H., Jaroszewicz, B., Joly, F.-X., Jucker, T., Koricheva, J., Milligan, H., Müller, S., Muys, B., Nguyen, D., Pollastrini, M., Raulund-Rasmussen, K., Selvi, F., Stenlid, J., Valladares, F., Vesterdal, L., Zielínski, D., Fischer, M., 2016. Jack-of-all-trades effects drive biodiversity–ecosystem multifunctionality relationships in European forests. Nat. Commun. 7, 11109. https://doi.org/10.1038/ncomms11109.

van Geffen, F., Heim, B., Brieger, F., Geng, R., Shevtsova, I.A., Schulte, L., Stuenzi, S.M., Bernhardt, N., Troeva, E.I., Pestryakova, L.A., Zakharov, E.S., Pflug, B., Herzschuh, U., Kruse, S., 2022. SiDroForest: a comprehensive forest inventory of Siberian boreal forest investigations including drone-based point clouds, individually labeled trees, synthetically generated tree crowns, and Sentinel-2 labeled image patches. Earth Syst. Sci. Data 14, 4967–4994. https://doi.org/10.5194/essd-14-4967-2022.

Verhegghen, A., Kuzelova, K., Syrris, V., Eva, H., Achard, F., 2022. Mapping canopy cover in African dry forests from the combined use of Sentinel-1 and Sentinel-2 data: application to Tanzania for the year 2018. Remote Sens. 14, 1522. https://doi.org/10.3390/rs14061522.

Vollrath, A., Mullissa, A., Reiche, J., 2020. Angular-based radiometric slope correction for Sentinel-1 on Google earth engine. Remote Sens. 12, 1867. https://doi.org/10.3390/rs12111867.

Waller, D., Amatangelo, K., Johnson, S., Rogers, D., 2013. Wisconsin vegetation database – plant community survey and resurvey data from the Wisconsin plant ecology laboratory. Biodiv. Ecol. 4, 255–264. https://doi.org/10.7809/b-e.00082.

Wang, Q., Ding, X., Tong, X., Atkinson, P.M., 2021. Spatio-temporal spectral unmixing of time-series images. Remote Sens. Environ. 259, 112407 https://doi.org/10.1016/j.rse.2021.112407.

Wang, J., Song, G., Liddell, M., Morellato, P., Lee, C.K.F., Yang, D., Alberton, B., Detto, M., Ma, X., Zhao, Y., Yeung, H.C.H., Zhang, H., Ng, M., Nelson, B.W., Huete, A., Wu, J., 2023. An ecologically-constrained deep learning model for tropical leaf phenology monitoring using PlanetScope satellites. Remote Sens. Environ. 286, 113429 https://doi.org/10.1016/j.rse.2022.113429.

Waser, L.T., Rüetschi, M., Psomas, A., Small, D., Rehush, N., 2021. Mapping dominant leaf type based on combined Sentinel-1/−2 data – challenges for mountainous countries. ISPRS J. Photogramm. Remote Sens. 180, 209–226. https://doi.org/10.1016/j.isprsjprs.2021.08.017.

Weinstein, B.G., Marconi, S., Bohlman, S., Zare, A., White, E., 2019. Individual tree-crown detection in RGB imagery using semi-supervised deep learning neural networks. Remote Sens. 11, 1309. https://doi.org/10.3390/rs11111309.

Wiegmann, S.M., Waller, D.M., 2006. Fifty years of change in northern upland forest understories: identity and traits of "winner" and "loser" plant species. Biol. Conserv. 129, 109–123. https://doi.org/10.1016/j.biocon.2005.10.027.

Wong, T.-T., Yeh, P.-Y., 2020. Reliable accuracy estimates from k-fold cross validation. IEEE Trans. Knowl. Data Eng. 32, 1586–1594. https://doi.org/10.1109/tkde.2019.2912815.

Wu, J., Kobayashi, H., Stark, S.C., Meng, R., Guan, K., Tran, N.N., Gao, S., Yang, W., Restrepo-Coupe, N., Miura, T., Oliviera, R.C., Rogers, A., Dye, D.G., Nelson, B.W., Serbin, S.P., Huete, A.R., Saleska, S.R., 2018. Biological processes dominate seasonality of remotely sensed canopy greenness in an Amazon evergreen forest. New Phytol. 217, 1507–1520. https://doi.org/10.1111/nph.14939.

Wu, S., Wang, J., Yan, Z., Song, G., Chen, Y., Ma, Q., Deng, M., Wu, Y., Zhao, Y., Guo, Z., Yuan, Z., Dai, G., Xu, X., Yang, X., Su, Y., Liu, L., Wu, J., 2021. Monitoring tree-crown scale autumn leaf phenology in a temperate forest with an integration of PlanetScope and drone remote sensing observations. ISPRS J. Photogramm. Remote Sens. 171, 36–48. https://doi.org/10.1016/j.isprsjprs.2020.10.017.

Xu, F., Cao, X., Chen, X., Somers, B., 2019. Mapping impervious surface fractions using automated Fisher transformed unmixing. Remote Sens. Environ. 232, 111311 https://doi.org/10.1016/j.rse.2019.111311.

Yang, X., Tang, J., Mustard, J.F., 2014. Beyond leaf color: comparing camera-based phenological metrics with leaf biochemical, biophysical, and spectral properties throughout the growing season of a temperate deciduous forest. J. Geophys. Res. Biogeosci. 119, 181–191. https://doi.org/10.1002/2013JG002460.

Yang, Y., Wu, T., Zeng, Y., Wang, S., 2021. An adaptive-parameter pixel Unmixing method for mapping Evergreen Forest fractions based on time-series NDVI: a case study of southern China. Remote Sens. 13, 4678. https://doi.org/10.3390/rs13224678.

Yang, D., Morrison, B.D., Hanston, W., McMahon, A., Baskaran, L., Hayes, D.J., Miller, C. E., Serbin, S.P., 2023. Integrating very-high-resolution UAS data and airborne imaging spectroscopy to map the fractional composition of Arctic plant functional types in Western Alaska. Remote Sens. Environ. 286, 113430 https://doi.org/10.1016/j.rse.2022.113430.

Yin, G., Li, A., Wu, S., Fan, W., Zeng, Y., Yan, K., Xu, B., Li, J., Liu, Q., 2018. PLC: a simple and semi-physical topographic correction method for vegetation canopies based on path length correction. Remote Sens. Environ. 215, 184–198. https://doi.org/10.1016/j.rse.2018.06.009.

Yommy, A.S., Liu, R., Wu, A.S., 2015. SAR image despeckling using refined Lee filter. In: Presented at the 2015 7th International Conference on Intelligent Human-Machine Systems and Cybernetics. IEEE. https://doi.org/10.1109/ihmsc.2015.236.

Zanaga, D., Van De Kerchove, R., Daems, D., De Keersmaecker, W., Brockmann, C., Kirches, G., Wevers, J., Cartus, O., Santoro, M., Fritz, S., 2022. ESA WorldCover 10 M 2021 v200.

Zhang, C., Ma, L., Chen, J., Rao, Y., Zhou, Y., Chen, X., 2019. Assessing the impact of endmember variability on linear spectral mixture analysis (LSMA): a theoretical and simulation analysis. Remote Sens. Environ. 235, 111471 https://doi.org/10.1016/j.rse.2019.111471.

Zhao, Y., Lee, C.K.F., Wang, Z., Wang, J., Gu, Y., Xie, J., Law, Y.K., Song, G., Bonebrake, T.C., Yang, X., Nelson, B.W., Wu, J., 2022a. Evaluating fine-scale phenology from PlanetScope satellites with ground observations across temperate forests in eastern North America. Remote Sens. Environ. 283, 113310 https://doi.org/10.1016/j.rse.2022.113310.

Zhao, F., Sun, R., Zhong, L., Meng, R., Huang, C., Zeng, X., Wang, M., Li, Y., Wang, Z., 2022b. Monthly mapping of forest harvesting using dense time series Sentinel-1 SAR imagery and deep learning. Remote Sens. Environ. 269, 112822 https://doi.org/10.1016/j.rse.2021.112822.

Zhong, Z., Li, J., Luo, Z., Chapman, M., 2018. Spectral–spatial residual network for hyperspectral image classification: a 3-D deep learning framework. IEEE Trans. Geosci. Remote Sens. 56, 847–858. https://doi.org/10.1109/tgrs.2017.2755542.

Zhuo, R., Fang, Y., Xu, L., Chen, Y., Wang, Y., Peng, J., 2022. A novel spectral-temporal Bayesian unmixing algorithm with spatial prior for Sentinel-2 time series. Remote Sens. Lett. 13, 522–532. https://doi.org/10.1080/2150704x.2022.2044087.